Title

Angular Momentum in Subbarrier Fusion: an Experimental Study using the Isomer Ratio {sup 137}Ce{sup m}/{sup 137}Ce{sup g}

Permalink

https://escholarship.org/uc/item/0762m7kd

Journal

Physical review C, 42(5)

Authors

DiGregorio, D.E.
Lesko, K.T.
Harmon, B.A.
et al.

Publication Date

1990-05-01

UC413

LBL-29003
Preprint

Lawrence Berkeley Laboratory
UNIVERSITY OF CALIFORNIA

Submitted to Physical Review C

Angular Momentum in Subbarrier Fusion: an Experimental Study using the Isomer Ratio $^{137}\mathrm{Ce}^{m}/^{137}\mathrm{Ce}^{g}$

D.E. DiGregorio, K.T. Lesko, B.A. Harmon, E.B. Norman,
J. Pouliot, B. Sur, Y. Chan, and R.G. Stokstad

May 1990

NUCLEAR SCIENCE DIVISION

Prepared for the U.S. Department of Energy under Contract Number DE-AC03-76SF00098.

LBL - 29003

Angular Momentum in Subbarrier Fusion: an Experimental Study using the Isomer Ratio $^{137}Ce^{m}/^{137}Ce^{g}$

D.E. DiGregorio, K.T. Lesko, B.A. Harmon, E.B. Norman,
J. Pouliot, B. Sur, Y. Chan, and R. G. Stokstad

Nuclear Science Division, Lawrence Berkeley Laboratory
1 Cyclotron Road, Berkeley, CA 94720

May 1990

This work was supported by the Director, Office of Energy Research, Division of Nuclear Physics of the Office of High Energy and Nuclear Physics of the U.S. Department of Energy under Contract DE-AC03-76SF00098

Angular Momentum in Subbarrier Fusion: an Experimental Study using the Isomer Ratio $^{137}Ce^{m}/^{137}Ce^{g}$

D.E. DiGregorio†, K.T. Lesko, B.A. Harmon§, E.B. Norman,
J. Pouliot*, B. Sur, Y. Chan, and R.G. Stokstad

Nuclear Science Division, Lawrence Berkeley Laboratory,
1 Cyclotron Road, Berkeley, CA 94720

ABSTRACT

The ratio of the yields for the isomer ($J^{\pi} = 11/2^{-}$, $t_{1/2} = 34.4$ h) and ground-state ($3/2^{+}$, 9.0 h) of ^{137}Ce populated in the reactions $^{128}Te(^{12}C,3n)$, $^{133}Cs(^{7}Li,3n)$, $^{136}Ba(^{3}He,2n)$, $^{136}Ba(^{4}He,3n)$, and $^{137}Ba(^{3}He,3n)$, were measured from energies above the Coulomb barrier to energies typically 20-30 % below the barrier by observing the delayed x- and γ-ray emission. In the first three reactions we observed an approximately constant value for the isomer ratio at energies far below the barrier. This indicates an approximately constant average angular momentum at low bombarding energies. We analyze isomer ratios and cross sections using a coupled channels model for the fusion and a statistical model for the decay of the compound nucleus. Absolute values of the angular momentum, $\bar{J}$, in the entrance channel are deduced from the isomer ratio. The values of $\bar{J}$ exhibit the behavior predicted for low energies and the expected variation with the reduced mass of the entrance channel.

PACS numbers: 25.70.Jj

I. Introduction

The enhancement of the measured fusion cross sections at energies below the Coulomb barrier relative to the predictions of the the one-dimensional barrier penetration model is a feature of all reactions induced by heavy ions [1-3]. Theoretical studies have shown how the nuclear structure of the colliding nuclei produces these enhancements [4-9]. A recent study of the fusion of ^{16}O with ^{144,147,149}Sm [10,11] together with earlier measurements on the other stable samarium isotopes [12] illustrates the importance of the shape degrees of freedom (nuclear deformation in this case) in describing the behavior of the fusion excitation functions. The influence on fusion of the coupling of the entrance channel to inelastic and to transfer channels in systems such as Ni + Ni [6,7] and ^{16}O + ^{208}Pb [8,9] has also been studied.

Experimental investigations of the distribution of angular momenta leading to fusion have provided important information that is complementary to the study of cross sections [13-18]. These measurements, primarily of gamma-ray multiplicity [13-16] and fission fragment angular distributions [17,18], have revealed the broadening of the spin distributions expected from the inclusion of the coupling of the entrance channel to structural and dynamical degrees of freedom. Some of these experiments have shown a much broader angular momentum distribution or a higher average angular momentum than predicted theoretically. This remains an outstanding problem in subbarrier fusion [19,20].

The relationship of the fusion cross section and the angular momentum in the entrance channel has not been studied at energies far below the Coulomb barrier where the cross sections are very small and the techniques mentioned above become difficult to apply. However, in this low energy region a qualitative change in the behavior of the average angular momentum has been predicted [21]. At and above the barrier the average angular momentum decreases as the bombarding energy is lowered. Below a certain energy, however, the shape of the distribution of angular momentum leading to fusion should no longer shift to lower l-values, but is predicted to become independent of energy [21]. Furthermore, the value of the average angular momentum, $\bar{l}$, is predicted to depend on the shape (i.e., on the curvature) of the barrier and on the reduced mass of the entrance channel, but should be independent of the nuclear structure of the projectile and target. These predictions are for the case of a parabolic barrier.

We have investigated these predictions - the constancy of $\bar{l}$ at low energies and the variation of $\bar{l}$ with the reduced mass - with an experimental technique that is different from those used previously [13-18]. Our method combines sensitivity to angular momentum with the ability to measure very small fusion cross sections. The latter is obtained through off-line counting of radioactivity. The former is achieved by taking advantage of the systematic occurrence of high spin isomers in heavy nuclei. Thus, by measuring the ratio of the cross section for population of a high spin isomeric state to that of a low spin ground state, we obtain the average angular momentum in the entrance channel [22,23] while, at the same time, through the observation of delayed x- and γ- rays, we are able to measure the small cross sections at which the saturation of the angular momentum is predicted to occur.

We measured the ratio of the isomer to ground-state yields of ^{137}Ce produced in the subbarrier fusion reactions ^{128}Te(^{12}C,3n)^{137}Ce, ^{133}Cs(^{7}Li,3n)^{137}Ce, and ^{136}Ba(^{3}He,2n)^{137}Ce. A partial decay scheme for the ground ($J^{\pi} = \frac{3}{2}^{+}$, $t_{1/2} = 9.0$ h) and isomeric ($\frac{11}{2}^{-}$, 34.4 h) states in ^{137}Ce is shown in Fig. 1. We deduced the predicted constant behavior of $\bar{l}$ at low energies and the expected variation with the reduced mass of the entrance channel from the observed variation of the isomer ratio with bombarding energy. The predicted angular momentum distributions, the cross sections for the 3n or 2n channels, and the isomer ratios were related to each other with the aid of a statistical model and found to be in agreement for energies at and below the barrier. Additional checks of this method were made by studying the reactions $^{137}Ba(^{3}He,3n)^{137}Ce$ and $^{136}Ba(^{4}He,3n)^{137}Ce$. A brief account of the measurements on the fusion of ^{128}Te with ^{12}C has been published [24].

We describe the experimental aspects of these measurements (Section II), the analysis of the delayed activity (Section III), and the results of these analyses (Section IV). In Section V we discuss the origin of a finite average angular momentum at low energies and the evidence for this from alpha radioactivity. This is followed in Section VI by a comparison of our results to theoretical predictions along with a discussion of the theoretical tools we employ to make these comparisons. (The details of the statistical model are given in an Appendix.) With these models in hand, we discuss in Section VII our methods for deducing the average angular momentum from the isomer ratio and, in Section VIII, the various checks we made on this procedure. Finally, in Section IX, we present a summary of our conclusions.

II. Experiments

The experiments were carried out with beams of ^{12}C, ^{7}Li, ^{3}He, and ^{4}He provided by the Lawrence Berkeley Laboratory's Electron Cyclotron Resonance ion source and 88-Inch Cyclotron. The beam energy is determined by a 120 ° analyzing magnet and is known to a precision of 0.1 %. Targets were made by vacuum deposition of isotopically enriched metallic tellurium (150-200 $\mu g/cm^2$, 98.7 % ^{128}Te), barium fluoride (250-300 $\mu g/cm^2$, 93 % ^{136}Ba), and natural cesium nitrate (300-400 $\mu g/cm^2$, 100 % ^{133}Cs), onto carbon or gold foils. (These foils were also used to catch the evaporation residues.) Some of the ^{136}Ba targets with thicknesses of 4-8 mg/cm^2, were prepared by applying a water solution of BaF_2 to gold foils with a micropipet, and letting the drops evaporate. The thicknesses of the targets and the catcher and degrader foils were determined by alpha-ranging and by using proton induced x-ray emission. The measurements of the tellurium and BaF_2 targets indicated that no detectable amount of material was lost during the bombardment. Target thicknesses thus determined had an uncertainty of less than 5 % and were used both for obtaining the absolute cross sections and for estimating the energy loss of the beam in the stack of foils. On the other hand, similar measurements of the cesium nitrate targets showed that some material was lost because of beam heating. Although this loss of material does not affect the determination of the isomer ratios, it prevents us from obtaining absolute cross sections for the ^{7}Li + ^{133}Cs reaction.

A series of target, catcher, and degrader foils were arranged in a stack to allow data collection at different energies in a single irradiation. The beam emerged from the stack and was stopped in a Faraday cup. The beam intensity during the bombardment was monitored and recorded by multiscaling in one minute intervals. Following bombardments of about eight hours at intensities of $\leq$ 200 nA, the target and catcher foils were removed from the scattering chamber and placed in front of high-purity intrinsic germanium detectors. The γ- and x-rays resulting from the activated foils were counted off-line for several days; spectra containing 2048 or 4096 channels were collected in one hour intervals. These spectra were accumulated and recorded automatically for off-line analysis by using IBM PC/AT computers. Fig. 2(a) shows a photon spectrum associated with the decay of the ground and isomeric states in ^{137}Ce produced in the fusion reaction ^{12}C + ^{128}Te at $E_{c.m.}$ = 42 MeV. This spectrum was counted for one hour beginning 28 minutes after the end of a bombardment of approximately eight hours. A portion of the spectrum that includes the La and Ce K_α and K_β x-rays is displayed in Fig. 2(b). The absolute photopeak efficiencies of the germanium detectors were obtained using a set of calibrated sources mounted in the same geometry as the target/catcher foils. At selected energies we verified that all the ^{137}Ce evaporation residues were stopped at the target/catcher foils and that all the relevant activity remained there. We also determined experimentally the average energy loss and straggling for the projectiles passing through the stack by detecting the beam particles with a silicon surface barrier detector placed at zero degrees, with and without the stack. The measured energy loss agreed well with that calculated from tabulated stopping powers and the measured foil thicknesses.

III. Data analysis

The ratio of the population of the isomeric state to the ground state can be obtained by measuring either the activities of the La K x-ray or the 447 keV γ-ray. Lanthanum K x-rays are produced mainly by electron capture to the 447 keV and 11 keV levels of the daughter nucleus ^{137}La. In addition, La x-rays are produced by internal conversion of the 447 keV transition with much less intensity. Ce x-rays are produced only by internal conversion of the 254 keV transition in ^{137}Ce, which depopulates the isomeric state directly to the ground state. Thus the Ce x-rays decay with a half-life of 34.4 h. Because ^{137}Ce decays mainly by electron capture and by highly converted electromagnetic transitions, the yield of x-rays per decay is much larger than the γ-ray yield. In the present measurements we summed the contributions from the partially resolved peaks of the La and Ce x-rays. Figure 3 shows the time evolution of the activities for the sum of La and Ce K x-rays for the systems ^{12}C + ^{128}Te and ^{3}He + ^{136}Ba at different bombarding energies. The isomer ratios and cross sections were deduced from these experimental data in a least-square fit incorporating the known half-lives and absolute x-ray intensities. The populations of the ground and isomeric states at the end of the bombardment were taken as adjustable parameters. These calculations were performed using the code XRAY [25]. The full curves in Fig. 3 are representative of the results for the different systems. The associated isomer ratios are given on the figure along with the bombarding energies.

In order to confirm that the atomic x-ray spectra were not contaminated by other species, similar analyses of the time dependence of nuclear γ-rays (447 keV for example) were made. The values of the isomer ratios were consistent with those obtained from the analysis of the K x-rays. Since at low energies the K x-rays were the only detectable radiation, these were used in the majority of the analyses. The absolute cross sections for the 3n or 2n channels were then determined from the measured target thickness, the integrated charge at the Faraday cup, and the absolute efficiency of the photon detector.

IV. Experimental results

The experimental results for the isomer ratios of the systems ^{12}C + ^{128}Te, ^{7}Li + ^{133}Cs, and ^{3}He + ^{136}Ba, are shown in Fig. 4 as a function of bombarding energy with respect to the corresponding Coulomb barrier. The isomer ratio, R, decreases rapidly as the bombarding energy is lowered and approaches the barrier. However, for energies well below the barrier the change in R with bombarding energy is much slower, and the isomer ratio for each reaction becomes nearly constant. The approximate constancy of R indicates that the ratio of cross sections for fusion proceeding through partial waves above and below some critical value has an approximately constant, energy independent value. Assuming (as is predicted by all fusion models) that the individual partial wave cross sections vary smoothly with energy, this result implies a constant average angular momentum for fusion. This conclusion is based on general knowledge of the role of angular momentum in the neutron and γ-ray decay of compound nuclei, and not on the details of a particular statistical model calculation.

The values of the isomer ratios for ^{7}Li and ^{12}C projectiles below the barrier are quite similar, indicating essentially the same constant average angular momentum.

The reason that the limiting average angular momentum for ^{7}Li fusion in this energy region is as large as for ^{12}C is due to the coupling of the ground state spins of $\frac{3}{2}$ and $\frac{7}{2}$ for ^{7}Li and ^{133}Cs, respectively. On the other hand, the limiting value of R and, therefore, the limit of the angular momentum obtained for ^{3}He, is substantially lower. This is because of the smaller moment of inertia in the entrance channel. Indeed, the observed dependence of R on the bombarding energy, on the ground state spins, and on the masses of the projectile and target indicates that the isomer ratio is a measure of the average angular momentum leading to fusion, and that this angular momentum approaches a constant at energies well below the barrier. A quantitative justification of this conclusion will be given in the sections VI and VII where model calculations are discussed.

Isomer ratios and absolute cross sections for the 3n and 2n channels were measured for ^{12}C + ^{128}Te and ^{3}He + ^{136}Ba, respectively, and are shown in Figs. 5 and 6. The results are presented in Tables I and II. Table III presents the experimental isomer ratios for ^{7}Li + ^{133}Cs. Note: the values of the cross sections for ^{12}C + ^{128}Te shown in Fig. 2 of Ref. 24 are too low by a factor of 1.9. This error arose from incomplete suppression of secondary electrons from the Faraday cup. The conclusions of Ref. 24 are not affected by this change in absolute normalization of the cross sections.

Isomer ratios and cross sections for some reactions reported here were first measured twenty-five years ago by Kiefer and Street [23]. While the isomer ratios obtained at the lowest energies studied by these authors agree reasonably well with ours, our values for ^{12}C+^{128}Te and ^{7}Li+^{133}Cs become comparatively larger with increasing bombarding energy. These discrepancies may arise from their use of NaI detectors (with their relatively poor energy resolution) and imprecisely known beam energies.

V. Origin of a finite average angular momentum at low energies

It is worthwhile to examine the predicted limiting behavior of the average angular momentum more generally, and to consider, for the case of a pure Coulomb barrier, the origin of a finite average angular momentum in the limit of very low bombarding energies. The capture of neutrons at very low energies has an s-wave limit, i.e., only thermal neutrons with $l = 0$ have an appreciable cross section. The reason for this is that, as the energy of the neutron decreases, it becomes progressively more difficult for the higher partial waves to penetrate the centrifugal barrier. Indeed, the ratio of the transmission coefficients for $l = 1$ and $l = 0$, $\frac{T_1}{T_0} \rightarrow kR_n$, for $kR_n \ll 1$, where k is the wave number and R_n is the nuclear radius [26]. Thus, for neutrons, the average angular momentum for fusion $\bar{l} \rightarrow 0$ as $E \rightarrow 0$. Since a centrifugal barrier is also present in the case of fusion with charged particles, one might expect a similar asymptotic behavior. In fact, however, the Coulomb barrier causes a qualitatively different dependence of the transmission coefficients on angular momentum and energy. It turns out that $\bar{l} \rightarrow l_0$, and that l_0 can be larger than unity ($\hbar$) for many systems, including the systems considered here. The reason is simply that the Coulomb contribution to the total barrier varies as $\frac{1}{r}$ and is the same for all partial waves including, in particular, the s-wave. The centrifugal potential, however, varies as $\frac{1}{r^2}$ and becomes relatively less important as the classically forbidden region extends to large values of r. If the Coulomb repulsion is sufficiently strong (i.e., if the barrier is sufficiently high and thick) and the moment of inertia of the system at the fusion radius, $\mu {R_n}^2$, is sufficiently large, then the contributions of the centrifugal potential to the total barrier for the lower partial waves can be sufficiently small that the ratio of $\frac{T_1}{T_0}$ remains finite. This implies a finite average angular momentum even at bombarding energies far below the barrier. These considerations are illustrated quantitatively for the case of a pure Coulomb barrier in the following.

The ratio of the height of the centrifugal barrier for $l = 1$, $V_{l=1} = \hbar^2/\mu R_n^2$ and the Coulomb barrier, $V_c = Z_1 Z_2 e^2/R_n^2$, is a measure of the relative importance of the centrifugal barrier, and is given by $\frac{V_{l=1}}{V_c} = 1/(\eta k R_n)$ where $\eta = Z_1 Z_2 e^2 / \hbar v$, is the Sommerfeld parameter and v is the velocity of the projectile. Then,

$$\frac{V_{l=1}}{V_c} = \frac{28.9}{\mu R_n Z_1 Z_2}$$

where the reduced mass μ is in AMU, and the nuclear radius R_n is in fm. Thus if $\frac{V_{l=1}}{V_c}$ is very small compared to unity we may expect a sizable average angular momentum at low energies. Values of $\frac{V_{l=1}}{V_c}$ for several systems and $R_n = 1.4 (A_1^{1/3} + A_2^{1/3})$ are given in Table IV. The ratio of the transmission coefficients for $l = 1$ and $l = 0$ for the case of charged particles far below the barrier has been evaluated with eq. 22.10 in Ref. 27:

$$\frac{T_l}{T_0} = \exp\left(-\frac{2\left(l+\frac{1}{2}\right)^2}{\sqrt{2 \eta k R_n}}\right). \tag{1}$$

Finally, the asymptotic values for the average angular momentum calculated using the approximate expression in Eq. 1 are listed in the last column of Table IV. They correspond to the penetration of a pure Coulomb-plus-centrifugal potential extending from a sharp nuclear surface at radius R to infinity.

The values in Table IV illustrate how the increasing strength of the Coulomb barrier relative to the centrifugal barrier introduces a finite average angular momentum for fusion.

The limiting value of the average angular momentum, and the manner in which it approaches the limit, depends on the actual shape of the potential. The potential given by a pure Coulomb force which terminates at a sharp nuclear surface, and the inverted parabolic potential used in the Hill-Wheeler approximation represent two extreme cases. The former has been used extensively in the treatment of alpha decay while the latter is a much more useful approximation for nuclear reactions in which the energy is necessarily closer to the maximum of the nuclear-plus-Coulomb potential. These two potentials also yield different results for the average angular momentum.

The penetrability for a given partial wave l incident on a potential having the shape of an inverted parabola is given by

$$T_l = \frac{1}{1 + \exp\left(\left[V_b + l(l+1)\hbar^2/2\mu R_b{}^2 - E\right] / \epsilon \right)}$$

where R_b is the radius corresponding to the top of the barrier V_b, and ϵ is related to the curvature of the barrier and is given by,

$$\epsilon = (\hbar/2\pi) \sqrt{-\frac{1}{\mu} \frac{\partial^2 V(R_b)}{\partial r^2}}.$$

As soon as the exponential factor is much larger than unity, the transmission coefficient is approximated by

$$T_l = \exp(-[V_b - E] / \epsilon) \exp(-[l(l+1)\hbar^2/2\mu R_b{}^2] / \epsilon)$$

In this limit the energy dependence and the angular momentum dependence are mutually independent factors, and the distribution of angular momentum becomes independent of bombarding energy, i.e., a constant. This energy dependence for the angular momentum is illustrated by the solid line in Fig. 7.

The values of $\bar{l}$ obtained for a pure Coulomb-plus centrifugal potential, evaluated with transmission coefficients calculated in the JWKB approximation [27] are also shown in Fig. 7 for $^{12}C+^{128}Te$ with $R_0 = 1.4$ fm (dot-dash line). Note that there is no sharp transition to a constant average value as in the case of the parabolic potential. The dashed curve shows the average angular momentum for a realistic potential consisting of nuclear, Coulomb and centrifugal contributions. Also note that this is similar to the dependence obtained with the inverted parabola in the bombarding energy range accessible to experiment.

For the relatively light nuclei (i.e., ^{12}C, ^{3}He, etc.) considered here, radioactive decay and fusion are processes that differ, not in the shape of the barrier to be penetrated, but only in the direction of penetration. Thus, the penetrability or transmission coefficients are the same for both processes as, indeed, we have already assumed in the foregoing discussion. We can turn to experimental results obtained in the study of alpha decay in order to understand the angular momentum dependence of fusion below the barrier. In the case of radioactive decay, it is possible to make observations at decay energies much further below the barrier than in the case of heavy ion reactions simply because experiments can be made on macroscopic quantities of atoms. While one cannot vary the decay energy arbitrarily, as in the case of a beam from an accelerator, it is possible to find nuclei having similar structure, but varying alpha decay energies. In contrast to a nuclear reaction, however, it is possible to specify exactly the value of the angular momentum in the decay.

It has been known from the earliest measurements of alpha decay that the ratio of the intensity of the d-wave decay to the s-wave decay varies slowly with the decay energy. One example of this is found in the decay of the neutron deficient thorium isotopes. Fig. 8 shows the ratio of the d and s wave intensities for the decay of $^{224-232}$Th [35]. The transition rates for the ground state decay, λ_0, are also shown as a function of decay energy. The corresponding theoretical quantities, T_0 and $\frac{T_2}{T_0}$, calculated for a radius parameter $R_0 = 1.55$ fm [35] are also shown. Note the close correspondence of $\frac{\lambda_2}{\lambda_0}$ with the theoretical ratio, $\frac{T_2}{T_0}$ over a span of half-lives varying by 17 orders of magnitude. (The ratio $\frac{\lambda_2}{\lambda_0}$ is affected by nuclear structure -

deformation in this case - as well as by barrier penetration. Although the deformations of parent and daughter nuclei change gradually with isotope, these effects on the absolute value of $\frac{\lambda_2}{\lambda_0}$ and on its variation with isotope can be neglected for the present discussion. Similarly, the relative agreement shown in Fig. 8, where T_0 is normalized at $E_\alpha = 8$ MeV, would have been just as satisfactory with $R_0 = 1.4$ fm.) If nature had also provided experimental values for the relative p, f, and g-wave transition rates, we would be able to determine an average angular momentum for alpha decay in direct analogy to that for fusion. It seems clear that such quantities would also vary slowly, as do the d-wave relative rates (Fig. 8) and that this situation corresponds to a finite, approximately constant average angular momentum, just as we have observed in heavy-ion fusion.

VI. Quantitative comparison of predictions with experiments

In order to compare theory and experiment it is necessary to relate a total cross section and a distribution of angular momentum for ^{140}Ce (or ^{139}Ce for one reaction) in the entrance channel to the 3n (or 2n) cross sections and isomer ratios for ^{137}Ce. This is done by means of a statistical model, which for a given excitation energy and angular momentum in the compound nucleus gives the probability that three (two) neutrons will be evaporated and that the subsequent γ-ray cascade will populate the isomer or the ground state. Combined with a model for fusion, which gives the total cross section and the initial distribution of angular momentum, the statistical model makes it possible to compare theory and experiment directly in terms of the *measured quantities.* This is done in the following two subsections. An alternative comparison in terms of the predicted average angular momentum will be discussed in section VII.

VI. a. Predictions for cross sections and the average angular momentum

In a recent paper, Dasso and Landowne [21] compared the predictions of coupled channels calculations to average angular momenta deduced from γ-multiplicity measurements at bombarding energies near and above the Coulomb barrier. A brief description of their calculation is as follows: By using the approximate solution of the general barrier penetration problem involving coupled channels i=1,...,N, the fusion cross section for a partial wave l at the bombarding energy E is given by,

$$\sigma_l(\mathrm{E}) = \frac{\pi \hbar^2}{2\mu \mathrm{E}} \sum_{\mathrm{i}} \mathrm{P_i} \frac{(2l+1)}{1 + \exp\left([\mathrm{V_b} + l(l+1)\hbar^2/2\mu \mathrm{R_b}^2 + \lambda_{\mathrm{i}} - \mathrm{E}] / \epsilon\right)} \qquad (2)$$

Equation (2) employs the Hill-Wheeler approximation for the penetration of an inverted parabolic barrier and treats the coupling as a sum of individual barrier penetration probabilities for each channel i with a barrier given by $\mathrm{V_i} = \mathrm{V_b}+\lambda_{\mathrm{i}}$, and weighted by the factor $\mathrm{P_i}$. The factor $\mathrm{P_i}$ corresponds to the fraction of the flux in that channel, and λ_{i} to the shift in the barrier height caused by the coupling. The Hill-Wheeler approximation neglects the $\frac{1}{\mathrm{r}}$ contribution of the Coulomb potential at large distances and also neglects changes in the shape of the barrier due to the centrifugal portion of the potential energy. As a result of the latter approximation, ϵ is a constant. The first moment of the angular momentum distribution is defined as,

$$\overline{l} = \frac{\sum_l l\, \sigma_l}{\sum_l \sigma_l}$$

At low energies $\mathrm{E} < \mathrm{V_b} - \mathrm{F}$, the spin distribution is independent of the bombarding energy and the corresponding $\overline{l}$ becomes a constant and is given by,

$$\overline{l} = (4/3)\sqrt{\mu \mathrm{R_b}^2 \epsilon / \hbar^2}.$$

The quantity F denotes the strength of the coupling. In the higher energy domain, where $\mathrm{E} > \mathrm{V_b} + \mathrm{F}$, the angular momentum distribution approaches a triangular shape and the $\bar{l}$ is approximately given by,

$$\bar{l} = (2/3)\sqrt{2\mu R_b^2 (E - V_b)/\hbar^2}$$

Within the energy range $V_b - F < E < V_b + F$, the shift of the barrier by λ_i results in an enhancement of $\bar{l}$ over the uncoupled case, particularly for heavy ion systems [21]. The measurements of average angular momentum [14] analyzed by Dasso and Landowne were made at energies too high to test the prediction of a constant average angular momentum.

Figure 9 shows partial wave distributions, σ_l, at a few energies for the fusion of ^{12}C with ^{128}Te. Below the barrier, the shape of the angular momentum distribution becomes essentially independent of the bombarding energy and is approximately symmetric about the average value $\bar{l}$; the total cross section decreases exponentially. For ^{12}C + ^{128}Te, the value of F is about 2 MeV. Above the barrier, the familiar triangular distribution for σ_l results, with $\bar{l}$ being two-thirds of the sharp-cutoff value for the maximum angular momentum, l_c,

$$\bar{l} = (2/3)\, l_c = (2/3)\sqrt{\sigma/\pi\lambdabar^2}$$

We have used the simplified coupled channels code (CCFUS) written by Dasso and Landowne [28], which is based on Eq. 2. The CCFUS code can treat coupling to collective excitations and to transfer channels. To calculate the penetrabilities, the matrix diagonalization method of Ref. 28 is used with the form of the nuclear potential determined by Christensen and Winther [29]. Because parameters for the barrier were not known from prior experiments, values of R_b and V_b for the systems C + Te, Li + Cs and He + Ba were scaled from the corresponding parameters determined from fusion experiments on ^{16}O + Sm [10]. Slight adjustments (less than 1.2 %) were made to the parameters for ^{12}C + ^{128}Te. Known electromagnetic transition probabilities for the lowest excited states of the projectile and target nuclei for each system, taken from the literature [30], were included in the calculations to account for the coupling effects. The barrier parameters for the three projectile-target combinations investigated here and the predicted values for $\bar{l}$ at energies well below the fusion barrier are given in Table V. The predicted cross sections are shown as full lines in Figs. 5(a) and 6(a).

Coupled channels calculations that treat the nuclear, Coulomb, and centrifugal potential and the radial dependence of the coupling matrix elements without approximation are possible, though difficult and time consuming. A comparison of CCFUS with the coupled channels code of Esbensen [31] using the same coupling and barrier parameters is shown in Fig. 7 along with the results from CCFUS for no coupling. In the subbarrier region, the solution of the coupled Schroedinger equations with the full Coulomb potential, yields a small monotonic decrease in the value of $\bar{l}$ as the bombarding energy decreases. This nonzero slope $d\bar{l}/dE$, which results from the $\frac{1}{r}$ tail of the Coulomb potential, was considered sufficiently small to justify the use of the CCFUS code for the analysis of our results.

VI. b. Statistical model calculations

In this section we describe the statistical model calculations used to establish the relationship between the spin distribution in the compound nucleus, formed through various entrance channels, and the relative populations of the ground and isomeric state in ^{137}Ce. To study this connection we used the predicted angular momentum distributions from CCFUS as input to a Hauser-Feshbach compound nucleus decay code. The latter treats the effects of successive evaporation of neutrons leading to the ^{137}Ce residue and the subsequent gamma-ray emission leading to the isomer or ground state. We chose the Monte Carlo code PACE [32] because of its explicit treatment of gamma-neutron competition. It also allows one to incorporate explicitly the low-lying levels of the residual nucleus and, thereby, treat the last steps of the γ-ray deexcitation more accurately than was possible with the earlier codes [22,23].

VI. b. 1. Input parameters

Wherever possible we adopted input parameters determined from analyses of previous experiments on similar systems. The fusion of ^{16}O with Sm isotopes has been studied extensively and xn partial cross sections are available [10-12]. A good fit to the xn distributions for the Sm isotopes was obtained using the level density parameter of $a = \frac{A}{8.5}$ and reduced gamma-transition strengths of 0.025, 0.01, 9. and 1.2 W.U. for the E1, M1, E2, and M2 transitions [11]. Most of the calculations presented in this work used the rigid body moments of inertia calculated by Sierk [33] for the spin cutoff factor in the level density formula of Gilbert and Cameron [34]. The remaining input parameters, such as the optical model parameters for transmission coefficients, were as described in Ref. 32. Whenever the ground state spin of an entrance channel nucleus was non-zero (^{7}Li $\frac{3}{2}$, ^{133}Cs $\frac{7}{2}$, ^{3}He $\frac{1}{2}$), the distribution of the total spin in the compound nucleus, $\vec{J} = \vec{l} + \vec{S}_1 + \vec{S}_2$, was computed and used in the evaporation calculation. A detailed discussion of the statistical model calculations, their sensitivity to variation of input parameters, and of the relationship of the angular momentum and isomer ratio is relegated to Appendix I.

VI. b. 2. Results of the calculations

The calculated isomer ratios for ^{12}C + ^{128}Te, ^{7}Li + ^{133}Cs, and ^{3}He +^{136}Ba are shown in Fig. 4. Figures 5(b) and 6(b) compare the calculated and measured isomer ratios for ^{12}C + ^{128}Te and ^{3}He +^{136}Ba as a function of the center of mass energy, along with the experimental results. The agreement of the calculations with the data is very good below the barrier.

We find that the isomer ratio has nearly the same value ($\simeq$ 1.5) for both the ^{12}C + ^{128}Te and ^{7}Li + ^{133}Cs systems, even though the average orbital angular momentum for a ^{7}Li projectile is less than for ^{12}C. This is a consequence of the spin coupling mentioned above, which introduces an extra spin angular momentum $\vec{S} = \frac{\vec{3}}{2} + \frac{\vec{7}}{2}$ in the case of ^{7}Li + ^{133}Cs. The intrinsic spin $\frac{1}{2}$ of ^{3}He nucleus does not significantly affect the predicted value of R ($\simeq$ 0.8) for ^{3}He + ^{136}Ba. Thus the predictions of CCFUS for $\bar{l}$ at low energies and the variation of $\bar{l}$ with the reduced mass below the barrier are consistent with the measured values of R, as shown in Fig. 4.

VII. Determination of the average angular momentum from the isomer ratio

The preceeding section has shown that the distribution of angular momentum predicted by a barrier penetration model is consistent with the experimentally observed isomer ratio. In this section we want to turn the problem around and, starting with the experimental value of the isomer ratio, determine a characteristic quantity of the distribution of the initial angular momentum without particular reference to a model for fusion. It is clear that this characteristic quantity will be the average value of the initial distribution. Our determination will be model independent to the extent that there is a one-to-one correspondence between the isomer ratio and the average angular momentum, i.e., that the deduced average is independent of the other, and unknown, moments of the distribution. In this process of relating the average angular momentum to the isomer ratio, we regard the statistical decay calculation, with the parameters determined as described in the preceding section and in Appendix I, as given.

The sensitivity of the isomer ratio to the average angular momentum was investigated by making two types of calculation. In the first type, a series of different distributions was used, all distributions having the same average value, but different shapes. These distributions, a triangle, a square, a delta function and a theoretical distribution deduced from a barrier penetration model at $E_{c.m.}$ = 35 MeV, are shown in Fig. 10. They have the same area and a fusion cross section of 0.143 mb. In the case of the square distribution this leads to a violation of unitarity for the lower partial waves, and for the delta function as well. However, this is irrelevant for the present discussion in which we are only concerned with the effect of the shape of the distribution on the resulting value of R. Table VI gives the results of calculations with PACE for each of the distributions shown in Fig. 10 for an excitation energy of 34 MeV in the compound nucleus, which corresponds to a center of mass bombarding energy of 35 MeV. Note that the fraction of the cross section in the 3n channel and the value of R are practically independent of the shape of the distribution. Similar results are obtained at $E_{c.m.} = 40.5$ MeV. If we repeat this procedure at $E_{c.m.} = 45$ MeV (5 MeV above the barrier energy) where the average angular momentum, 12$\hbar$ is twice that of the isomer, we observe a wider range in the values of R obtained for different distributions having the same average value. However, the values obtained for the sharp-cutoff, square, and barrier-penetration distributions still differ by less than 16 %.

The second type of calculation determines how the isomer ratio varies with the average angular momentum, again for a fixed compound nucleus excitation energy. In this calculation we used a Fermi function defined as,

$$T_l = \frac{1}{1 + \exp\left[(l - l_0)/\Delta l \right]}$$

for the shape of the initial spin distribution with fixed Δl and variable l_0. The results are shown in Fig. 11 (solid lines) for $E_{c.m.} = 35$ and 40.5 MeV along with the experimental values of R. Neglecting any contribution to the total error from uncertainties in the statistical model parameters, the values of the average angular momentum corresponding to the experimental isomer ratio are $5.4 ^{+0.6}_{-1.0}$ and 7.2 ± 0.4 $\hbar$, respectively. We deduce a value of $\bar{l} = 11.8 \pm 0.5$ $\hbar$ at $E_{c.m.} = 45$ MeV. Our estimates of the average angular momenta at the three bombarding energies, when uncertainties in the statistical model are taken into account, are $5.4^{+0.7}_{-1.1}\,\hbar$, $7.2^{+0.6}_{-0.8}\,\hbar$, and $11.8^{+0.8}_{-1.0}\,\hbar$.

This procedure to determine the average angular momentum (use of a Fermi function for the shape of the initial distribution with fixed Δl and variable l_0) has been repeated for all three systems. A smooth curve was drawn through the experimental values of the isomer ratios. Values from this curve were then converted into angular momentum at selected energies. The results are given in Figs. 12-14. Note the constant value of the angular momentum obtained at the lowest energies in each of these three systems.

VIII. Additional reactions

In addition to the reactions described above we have also measured the isomer ratios and the 3n cross sections produced in the fusion reactions ^{137}Ba(^{3}He,3n)^{137}Ce and ^{136}Ba(^{4}He,3n)^{137}Ce in the bombarding energy range $E_{c.m.}$ = 18.5-24.8 MeV and $E_{c.m.}$ = 33.2-36.9 MeV, respectively. The results are summarized in Tables VII and VIII. These measurements were used as an independent check of the absolute angular momentum by measuring the absolute cross section well above the Coulomb barrier (V_b is approximately 16 MeV for both systems). All calculations indicate that the angular momentum distribution has a triangular shape in this energy region. Thus by using the smooth-cutoff approximation one can determine an independent absolute value for the angular momentum by measuring the absolute fusion cross section. The bombarding energy ranges were selected so that the 3n channel leading to ^{137}Ce exhausts between 75-95 % of the total fusion cross section. In addition, the ^{3}He +^{137}Ba system populates the same excitation energy and angular momentum in the compound nucleus as does ^{12}C +^{128}Te at the bombarding energies used in the previous measurements. Fig. 15 displays and summarizes the deduced values of $\bar{J}$ as a function of the excitation energy in the compound nucleus ^{140}Ce (or ^{139}Ce for one reaction) for all systems studied in the present work.

For the ^{4}He + ^{136}Ba the values of $\bar{l}$ obtained from the the isomer ratio and from the smooth-cutoff analysis of the cross sections (in parenthesis) are 9.5 ± 0.4 (9.8 ± 0.7), 9.8 ± 0.5 (10.4 ± 0.8) and 10.2 ±0.5 (10.7 ± 0.8) $\hbar$ at $E_{c.m.}$ = 33.2, 35.1 and 36.9 MeV, respectively.

The same approach in the ^{3}He + ^{137}Ba reaction (and including the ground-state spins of ^{3}He and ^{137}Ba) gave values of 5.0 ± 0.5 (4.8 ± 0.4), 5.3 ± 0.5 (4.8 ±0.4), and 5.7 ± 0.6 (5.4 ± 0.4) $\hbar$ at $E_{c.m.}$ = 21.5, 22.8, and 24.9 MeV, respectively.

We have also extended this study of the average angular momentum for fusion using the reaction ^{186}W(^{12}C,3n)^{195}Hg. The ratio of the population of the isomeric ($J^{\pi} = 13/2^{+}$) and ground ($1/2^{-}$) states in ^{195}Hg also exhibits an energy dependence characteristic of a constant average angular momentum in the entrance channel below the barrier (see Fig. 16). The analysis is still in progress. However, the constant $\bar{l}$ observed for subbarrier fusion leading to a system with different mass and spins than ^{137}Ce indicates the universality of this phenomenon.

IX. Summary

We have measured the ratio of the yields for the isomer ($J^{\pi} = 11/2^{-}$, $t_{1/2}$ = 34.4 h) and ground-state ($3/2^{+}$, 9.0 h) of ^{137}Ce produced in the subbarrier fusion reactions ^{128}Te(^{12}C,3n), ^{133}Cs(^{7}Li,3n), and ^{136}Ba(^{3}He,2n), by observing the delayed x- and γ-rays emitted in the decay of these states. We deduced the average angular momentum, $\bar{J}$, from the experimentally isomer ratio with a statistical model. The values of $\bar{J}$ thus obtained exhibit the predicted behavior of the average angular momentum at low energies and the expected variation with the reduced mass of the entrance channel. The isomer ratio technique can be an important tool for determining the average angular momentum in subbarrier fusion. These measurements are of interest because they provide an independent experimental approach to the problem, recently pointed out by Vandenbosch [19], that for energies below the barrier theoretical values of the average angular momentum frequently disagree with those deduced from γ-ray multiplicities and fission fragment angular correlations.

Acknowledgments

We are pleased to acknowledge a number of helpful discussions with R. Vandenbosch. We thank H. Esbensen for performing coupled channel model calculations for the $^{12}C + ^{128}Te$ system. This work was supported by the Director, Office of Energy Research, Office of High Energy and Nuclear Physics, Nuclear Physics Division, of the U.S. Department of Energy under contract DE-AC03-76SF00098.

Appendix I

I. a. Relationship of angular momentum and isomer ratio

The statistical-decay model enables an examination of the sensitivity of the isomer ratio to the initial angular momentum distribution in the compound nucleus and, of course, to the parameters (level density, moment of inertia, etc.) that govern the neutron and gamma-ray decay. The sensitivity of the isomer ratio to the angular momentum distribution in the entrance channel is illustrated in Fig. 17. The results of three types of predictions for $^{12}C + ^{128}Te$ are shown there, along with the experimental isomer ratios. The horizontal bars give the isomer ratio produced by decay of a compound nucleus having a unique angular momentum and excitation energy. Thus, ^{140}Ce nuclei produced in a collision at $E_{c.m.} = 37$ MeV and having a total angular momentum of 6 ħ would, after decay, produce an isomer ratio of about 3, whereas similar nuclei having an angular momentum of zero ħ would produce an isomer ratio of only 0.4. The dashed line is the isomer ratio resulting from a triangular, sharp-cutoff distribution with a total fusion cross section given by Eq. 3. The solid curve is the same calculation as shown in Fig. 5. These calculations show that the isomer ratio is quite sensitive to the compound nucleus angular momentum, particularly for values comparable to the spin of the isomeric level. Fig. 17 thus shows that the isomer-ratio method is capable of testing whether the average angular momentum leading to fusion becomes constant below the barrier or continues to decrease.

I. b. Spin Fractionation

Only those collisions that lead to the 3n channel (or the 2n channel in the case of ^{3}He + ^{136}Ba) provide information on the angular momentum, since the isotopes on either side of ^{140}Ce are stable. This introduces a bias in the measurement, because the angular momentum influences the number of neutrons emitted, an effect referred to as spin fractionation. Figure 18(a) shows the predicted relative intensities of the 2n, 3n, and 4n channels for ^{12}C + ^{128}Te. The 3n channel is the strongest over the energy region in which the average angular momentum is expected to be constant. This minimizes the effect of spin fractionation, and is one of the reasons why this particular system was chosen for this study.

The effect of spin fractionation and the consequences of neutron evaporation on the average angular momentum are illustrated in Fig. 18(b). The full line is the predicted average angular momentum in the compound nucleus. If in the Monte Carlo calculation we select from all partial waves only those that eventually populate the 3n channel, and calculate their average angular momentum, the dashed line is obtained. At higher energies in the fusion entrance channel the evaporation of four neutrons preferentially removes the lower partial waves resulting in an increase of the average of the spin distribution for the 3n exit channel. Conversely at lower energies the evaporation of two neutrons results in the lowering of the average spin. Overall, spin fractionation has a small effect on the observed average of the spin distribution and it vanishes in the vicinity of the Coulomb barrier at $E_{c.m.} = 40$ MeV, where the 3n cross section is at a relative maximum and the point at which $\bar{l}$ is becoming a constant. The dash-dot line in the figure is the average angular momentum of the ^{137}Ce nucleus before emission of any gamma rays, i.e., the entry-state average angular momentum. The difference between the dashed line and dash-dot line is the average angular momentum removed by neutrons. Again, this is not a large effect, and we see that, above 40 MeV bombarding energy, it cancels the effect of fractionation. Of course, all these effects are automatically taken into account when the statistical model is used to predict the isomer ratio from an initial angular momentum distribution.

We are now in a position to investigate the predicted slow decrease of the isomer ratio for bombarding energies below 38 MeV, even when the input average angular momentum is a constant (Figs. 4, 5(b), 6(b), 12, 13 and 14). This slow decrease is a consequence of three factors. The first is the decreasing excitation energy in the compound nucleus (at constant angular momentum). This effect is easily seen in Fig. 17. The second factor is spin fractionation (Fig. 18(b)). An additional factor that would contribute to a decrease in the value of R at lower energies is a continued decrease in the average angular momentum, as is predicted to occur when the full nuclear-plus-Coulomb potential is used instead of a parabolic approximation. However, the difference in the predicted slopes of $\bar{l}$ in the region 35 - 40 MeV is too small to be detected in this experiment.

I. c. Discrete low lying levels

The level density in the statistical model for the initial population in ^{137}Ce from the entry point to 2 MeV of excitation energy is approximated with the usual formulae [32]. Below 2 MeV excitation energy, individual discrete states are used. Clearly, the absolute value of the isomer ratio can depend sensitively on the final stages of the gamma-ray decay and it is a distinct advantage to be able to use discrete states in the calculation. The principal sources of information on the level scheme of ^{137}Ce are Refs. 36-38. Low-spin levels have been studied in the radioactive decay of ^{137}Pr [36] and thermal neutron capture in ^{136}Ce [37], and high spin levels (in the band built on the isomer) in the (alpha,xn) reaction [38]. These three methods, however, do not reveal the intermediate spin states, levels with $\frac{7}{2}$ and $\frac{9}{2}$. Since such levels must be present, we therefore added some states with appropriate spins and excitation energies to the calculation. The choices of spins and excitation energies represented a reasonable interpolation of the trends in level density for the low and high spin regions. (We also were guided in the placement of these intermediate spin levels by the level scheme for ^{123}Sn, which has an $\frac{11}{2}^-$ ground state and a shell-model configuration of three neutrons in the $h_{11/2}$ shell. ^{137}Ce, has a structure of three neutron holes in a filled $h_{11/2}$ shell.) The known and added states below 2 MeV that were used in the final calculations of the isomer ratio are shown in Fig. 19.

Figure 20(a) shows the effects on the isomer ratio of different treatments of the level structure below 2 MeV. Figure 20(b) shows the density of levels corresponding to these different combinations. If the low lying structure is represented by a level density formula, and only the ground and isomeric states are considered explicitly, the dashed curve in Fig. 20(a) is obtained. If only the known discrete states below 2 MeV are included, the isomer ratio given by the dash-dot line results. Including an extra six levels of intermediate spin results in the full curve. Inclusion of these extra levels in the calculation increased the decay to the ground state, and thus lowered the predicted isomer ratio. Including another 8 states (for a total of 14 extra states) made no significant difference in R and calculations were conducted with only 6 extra states. Note that even the difference in the isomer ratio calculated with only the known states and with the six extra states is quite small.

Because of their intermediate spins, the low-lying lying $\frac{7}{2}$ and $\frac{9}{2}$ levels in ^{137}Ce represent a dividing point for gamma-ray transitions eventually leading to the isomer or to the ground state. Depending on the relative energies and on the parities, either a $\frac{7}{2}$ or a $\frac{9}{2}$ level could shift the gamma-ray intensity passing through it entirely to the ground state or to the isomer. An upper limit on the uncertainty in the predicted isomer ratio arising from a lack of knowledge of the details of the level scheme can be estimated, therefore, by determining (in the calculation) the number of transitions feeding the lowest $\frac{7}{2}$ state (one of the six states added to the level scheme). At $E_{c.m.} = 38$ MeV, this is about 5% of all compound nuclear decays. If all of the decays of this state were to go to the isomer, instead of to the ground state, the calculated isomer ratio would increase from 2.0 to 2.6 and the deduced $\mathcal{I}$ would decrease from 5.6 h to 4.5 h. Table IX. shows for three bombarding energies the changes in the deduced $\mathcal{I}$ when the decay of the $\frac{7}{2}$ state is switched to the isomer. These uncertainties may be reduced at a future time if a more complete level scheme is determined.

I. d. The Moment of inertia

A sensitive parameter in the statistical calculation, as has been pointed out previously [22,23], is the moment of inertia. Figure 19 shows the yrast lines corresponding to the different moments of inertia used in the calculations. The yrast lines specified by both Gilbert-Cameron [34] and Sierk [33] are consistent with the positions of the known yrast states above the isomer in ^{137}Ce. We take the Gilbert-Cameron theoretical yrast line as a reasonable limit for the upper location of the yrast line appropriate for this calculation. At $E_{c.m.} = 38$ MeV, changing from the Sierk to the Gilbert-Cameron yrast line changes the calculated isomer ratio from 2.0 to 1.7. This would change the deduced $\bar{l}$ from 5.6 h to 6.4 h. Table IX. gives the corresponding changes in angular momentum at three energies. The combined errors given in the main text were computed by adding in quadrature the error from the uncertainty in the isomer ratio with one-half the maximum change in $\bar{J}$ associated with the change of the yrast line or the decay of the $\frac{7}{2}$ state.

References

† Permanent address: Departamento de Fisica-TANDAR, Comisión Nacional de Energia Atómica, 1429 Buenos Aires, Argentina and CONICET.

§ Present address: Space Science Laboratory, NASA-Marshall Space Flight Center, Huntsville, AL 35812.

* Present address: GANIL, BP 5027, 14201 Caen Cedex, France.

1. R.G. Satchler, Proc. on the XII Workshop on Nuclear Physics, Iguazu Falls, Argentina, 1989, World Scientific Publishing Co, (to be published), and references therein.
2. M. Beckerman, Phys. Rep. **129**, 145 (1985).
3. S.G. Steadman and M.J. Rhodes-Brown, Ann. Rev. Nucl. Part. Sci. **36**, 649 (1986).
4. H. Esbensen, Nucl. Phys. **A352**, 147 (1980).
5. C. H. Dasso, S. Landowne and A. Winther, Nucl. Phys. **A405**, 318 (1983), Nucl. Phys. **A407**, 221 (1983), Nucl. Phys. **A432**, 495 (1985),
6. R.A. Broglia, C.H. Dasso, S. Landowne and G. Pollarolo, Phys. Lett. **B133**, 34 (1983).
7. R.A. Broglia, C.H. Dasso and S. Landowne, Phys. Rev. **C32**, 1426 (1985).
8. S.C. Pieper, M.J. Rhodes-Brown, and S. Landowne, Phys. Lett. **B162**, 43 (1985).
9. I.J. Thompson, M.A. Nagarayan, J.S. Lilley, and B.R. Fulton, Phys. Lett. **B157**, 250 (1985).
10. D.E. DiGregorio, J.O. Fernández Niello, A.J. Pacheco, D. Abriola, S. Gil, A.O. Macchiavelli, J.E. Testoni, P.R. Pascholati, V.R. Vanin, R. Liguori Neto, N. Carlin Filho, M.M. Coimbra, P.R.S. Gomes and R.G. Stokstad, Phys. Lett. **B176**, 322 (1986).

11. D.E. DiGregorio, M. diTada, D. Abriola, M. Elgue, A. Etchegoyen, M.C. Etchegoyen, J.O. Fernández Niello, A.M.J. Ferrero, S. Gil, A.O. Macchiavelli, A.J. Pacheco, J.E. Testoni, P.R.S. Gomes, V.R. Vanin, R. Liguori Neto, E. Crema, and R.G. Stokstad, Phys. Rev. **C39**, 516 (1989).

12. R.G. Stokstad, Y. Eisen, S. Kaplanis, D. Pelte, U. Smilansky and I. Tserruya, Phys. Rev. Lett. **41**, 465 (1978); Phys. Rev. **C21**, 2427 (1980).

13. S. Gil, R. Vandenbosch, A.J. Lazzarini, D.-K. Lock and A. Ray, Phys. Rev. **C31**, 1752 (1985).

14. B. Haas, G. Duchene, F.A. Beck, T. Byrski, C. Gehringer, J.C. Merdinger, A. Nourredine, V. Rauch, J.P. Vivien, J. Barrette, S. Tobbeche, E. Bozek, J. Styczen, J. Keinomen, J. Dudek, and W. Nazarewicz, Phys. Rev. Lett. **54**, 398 (1985).

15. P.J. Nolan, D.J.G. Love, A. Kirwan, D.J. Unwin, A.H. Nelson, P.J. Twin, J.D. Garret, Phys. Rev. Lett. **54**, 2211 (1985).

16. M.L. Halbert, J.R. Beene, D.C. Hensley, K. Honkanen, T.M. Semkow, V. Abenante, D.G. Sarantities, and Z. Li, Phys. Rev. **C40**, 2558 (1989).

17. R. Vandenbosch, T. Murakami, C.-C. Sahm, D.D. Leach, A. Ray and M.J. Murphy, Phys. Rev. Lett. **56**, 1234 (1986).

18. T. Murakami, C.-C. Sahm, R. Vandenbosch, D.D. Leach, A. Ray and M.J. Murphy, Phys. Rev. **C34**, 1353 (1986).

19. R. Vandenbosch, Proceedings of Symposium on Heavy Ion Interactions around the Coulomb Barrier, Legnaro, Italy, June 1988, edited by C. Signorini et al., Lecture Notes in Physics Vol. 317, 157 (Springer-Verlag, 1988).

20. C.H. Dasso, H. Esbensen, and S. Landowne, Phys. Rev. Lett. **57**, 1498 (1986).

21. C.H. Dasso and S. Landowne, Phys. Rev. **C32**, 1094 (1985).

22. R. Vandenbosch and J.R. Huinzenga, Phys. Rev., **120**, 1313 (1960); H. Warhanek and R. Vandenbosch, J. Inorg. Nucl. Chem., **26**, 669 (1964).

23. R.L. Kiefer and K. Street, Jr., Phys. Rev. **173**, 1202 (1968); R.L. Kiefer, PhD Thesis, University of California, UCRL-11049 (1963).

24. R.G. Stokstad, D.E. DiGregorio, K.T. Lesko, B.A. Harmon, E.B. Norman, J. Pouliot, and Y.D. Chan, Phys. Rev. Lett. **62**, 399 (1989).

25. A.J. Pacheco, D.E. DiGregorio, J.F. Fernández Niello and M. Elgue, Comput. Phys. Commun. **52**, 93 (1988).

26. J.M. Blatt and V.F. Weiskopf, *Theoretical Nuclear Physics*, (John Wiley and Sons, Inc., New York, 1952), p. 361.

27. I. Perlman and J.O. Rasmussen, Alpha Radioactivity, in Handbuch der Physik, **42**, 143 (1957).

28. C.H. Dasso and S. Landowne, Phys. Lett. **B183**, 141 (1987); Comp. Phys. Comm. **46**, 187 (1987).

29. P.R. Christensen and A. Winther, Phys. Lett. **B65**, 19 (1976).

30. S. Raman, C.H. Malarkey, W.T. Milner, C.W. Nestor, Jr., and P.H. Stelson, Atomic Data and Nucl. Data Tables, **36**, 1 (1987); H. Massman and J.O. Rasmussen, Nucl. Phys. **A243**, 155 (1975); Yu. V. Sergeenkov and V. M. Sigalov, Nucl. Data Sheets, **49**, 639 (1986).

31. H. Esbensen, private communication.

32. A. Gavron, Phys. Rev. **C21**, 230 (1980).

33. A. Sierk, Phys. Rev. **C33**, 2039 (1986).

34. A. Gilbert and A.G.W. Cameron, Can. J. Phys. **43**, 1446 (1965).

35. P. Hornshoj, P.G. Hansen, B. Jonson, H.L. Ravn, L. Westgaard, and O.B. Nielsen Nucl. Phys. **A230**, 365 (1974)

36. V. S. Buttsev et al., Izv. Akad. Nauk SSSR, Ser. Fiz. **37** 938 (1973); Bull. Acad. Sci. USSR Phys. Ser **37**, 26 (1974).

37. L.K. Peker, Nucl. Dat. Sheets. **38**, 87 (1983).

38. M. Mueller-Veggian, et al., Nucl. Phys. **A304**, 1 (1978).

Table I. Isomer Ratios and 3n-Cross Sections for $^{12}C + ^{128}Te$.

$E_{c.m.}$ [MeV]	R from x-ray	R from 447 keV	σ_{3n} [mb]
49.9±0.1			196.±30.
48.4±0.1			316.±45.
47.4±0.15			325.±50.
47.0±0.1	34.1±4.8	37.9±6.7	
45.6±0.15			325.±50.
44.9±0.1	17.5±1.9		340.±50.
44.5±0.1	14.8±1.0	16.0±1.2	
42.7±0.2	6.1±0.3		243.±35.
42.3±0.15	5.5±0.3		236.±35.
42.0±0.1	5.8±0.2	6.1±0.4	254.±40.
41.9±0.1	5.7±0.2	6.2±0.4	231.±35.
40.7±0.1	3.8±0.15	3.7±0.2	
40.4±0.2	3.4±0.1	3.3±0.2	157.±25.
39.7±0.2	3.3±0.4		107.±15.
39.4±0.15	2.4±0.15	1.9±0.6	76.±10.
39.0±0.15	2.2±0.15	2.3±0.15	61.±10.
38.0±0.15	1.5±0.1		15.8±2.4
37.5±0.2	1.5±0.1	1.2±0.3	7.9±1.2
36.9±0.1	1.7±0.15	2.3±0.6	4.2±0.6
36.0±0.2	1.4±0.1		1.22±0.18
35.6±0.2	1.5±0.3		0.26±0.04
35.0±0.2	1.3±0.4		0.14±0.02
34.5±0.1	1.6±0.4		0.037±0.006

The errors include statistical and estimated systematic errors.

Table II. Isomer Ratios and 2n-Cross Section for ^{3}He + ^{136}Ba.

$E_{c.m.}$ [MeV]	R from x-ray	R from 447 keV	σ_{2n} [mb]
23.4±0.1	2.0±0.1	2.4±0.5	100.±15.
22.5±0.6	1.9±0.1	2.2±0.2	73.±15.
21.1±0.1	1.8±0.09		110.±17.
20.3±0.9	1.8±0.09	1.9±0.1	124.±25.
18.8±0.5	1.7±0.09	1.8±0.15	132.±20.
17.9±1.1	1.4±0.07	1.4±0.1	75.±15.
17.4±0.5	1.4±0.07	1.4±0.08	73.±15.
16.2±0.5	1.1±0.06	1.3±0.09	104.±16.
15.6±1.1	1.0±0.05		49.±12.
14.1±0.8	0.74±0.06	0.74±0.13	22.4±4.5
12.8±0.9	0.61±0.05		10.1±2.0
11.5±1.0	0.51±0.04		1.78±0.45

The errors include statistical and estimated systematic errors.

Table III. Isomer Ratios for ^{7}Li + ^{133}Cs.

$E_{c.m.}$ [MeV]	R from x-ray	R from 447 keV
28.7±0.09	8.3±1.2	10.3±2.1
27.8±0.10	9.2±1.4	5.9±0.7
27.3±0.11	5.8±0.3	
27.2±0.12	7.0±1.1	6.7±0.6
26.6±0.09	5.4±0.6	4.7±0.5
25.9±0.13	5.3±0.5	5.1±0.5
24.4±0.15	3.8±0.2	3.9±0.4
23.8±0.15	3.3±0.3	3.8±0.4
23.0±0.12	2.6±0.2	2.4±0.3
22.8±0.10	2.5±0.15	2.6±0.15
21.9±0.10	2.5±0.15	2.6±0.15
21.7±0.15	2.1±0.15	2.3±0.3
21.2±0.17	2.0±0.12	
20.5±0.18	1.6±0.1	1.8±0.15
20.0±0.18	1.5±0.1	
19.5±0.15	1.5±0.1	1.2±0.3
19.0±0.20	1.6±0.1	
18.6±0.20	1.5±0.1	
18.5±0.15	1.4±0.14	1.5±0.3
17.8±0.15	1.7±0.17	

The errors include statistical and estimated systematic errors.

Table IV. Barrier ratios, penetrability ratios, and average angular momenta for different systems, calculated for a pure Coulomb potential, as the bombarding energy approaches zero.

System	$\frac{V_{l=1}}{V_c}$	$\frac{T_1}{T_0}$	$\bar{l}$ [$\hbar$]
^{4}He + ^{4}He	0.81	0.06	0.15
^{3}He + ^{136}Ba	9.5 x 10^{-3}	0.73	1.8
^{12}C + ^{128}Te	8.2 x 10^{-4}	0.91	3.9

Table V. List of parameters for CCFUS calculations. The position, height, and width of the barrier, and the average angular momentum and total spin used for the three indicated systems.

System	R_b [fm]	V_b [MeV]	$\hbar w$ [Mev]	$\bar{l}$ [$\hbar$]	$\bar{J}$ [$\hbar$]
^{12}C + ^{128}Te	10.70	39.4	4.37	5.3	5.3
^{7}Li + ^{133}Cs	10.09	22.0	4.26	3.7	5.5
^{3}He + ^{136}Ba	9.42	15.9	5.63	2.5	2.6

Table VI. Statistical model calculations for ^{12}C + ^{128}Te at $E_{c.m.}$ = 35 MeV using input angular momentum distributions having approximately the same $\bar{l} = 5.3\ \hbar$, but different shapes (Fig. 10).

Shape	l_0 [$\hbar$]	Δl [$\hbar$]	$\bar{l}$ [$\hbar$]	Width [$\hbar$]	R	3n [%]
Delta function	-	-	5.3	0	1.44	72.9
Rectangle	-	-	5.5	2.3	1.54	70.9
Fermi (s-c)	8.0	0.01	5.2	2.0	1.54	73.0
Fermi	5.4	1.8	5.3	3.0	1.33	71.6
CCFUS	-	-	5.3	3.0	1.31	71.0

Table VII. Isomer Ratios and 3n-Cross Sections for ^{4}He + ^{136}Ba.

$E_{c.m.}$ [MeV]	R from x-ray	R from 447 keV	σ_{3n} [mb]
36.9±0.1	7.8±0.4	8.4±0.5	1200.±180.
35.1±0.1	6.6±0.3	6.5±0.4	1115.±170.
33.2±0.1	5.6±0.3	5.4±0.3	880.±130.

The errors include statistical and estimated systematic errors.

Table VIII. Isomer Ratios and 3n-Cross Sections for ^{3}He + ^{137}Ba.

$E_{c.m.}$ [MeV]	R from x-ray	R from 447 keV	σ_{3n} [mb]
24.9±0.1	2.8±0.2	2.7±0.3	520.±105.
22.8±0.1	2.1±0.2	2.4±0.3	450.±90.
21.5±0.1	1.7±0.1	1.7±0.4	445.±90.
20.3±0.1	1.5±0.1	1.5±0.4	333.±66.
18.5±0.1	1.2±0.1	1.3±0.2	264.±55.

The errors include statistical and estimated systematic errors.

Table IX. Uncertainties in the deduced average angular momentum.

$E_{c.m.}$ [MeV]	$\bar{l}$ [ħ]	Experimental uncertainty in R [ħ]	Replace Sierk by G-Cameron [ħ]	Switch $\frac{7}{2}$ state decay to isomer [ħ]	Combined error [ħ]
35.0	5.4	+0.6 -1.0	+0.7	-1.1	+0.7 -1.1
40.5	7.2	±0.4	+0.9	-1.5	+0.6 -0.8
45.0	11.8	±0.5	+1.2	-1.8	+0.8 -1.0

Figure 1. A partial level scheme of ^{137}Ce showing the decay of the isomer at 254 keV and the ground-state.

Figure 2. A typical spectrum of delayed activity obtained with high-purity Ge detectors. γ-rays are labelled with the decay energy (in keV) and the parent nucleus in a). The region of the spectrum containing the x-rays is expanded in b).

Figure 3. Representative decay curves of x-rays formed in the bombardment of ^{128}Te targets with ^{12}C and of ^{136}Ba targets with ^{3}He at the indicated beam energies. The curves are the results of fitting the data using the code XRAY [25]. The isomer ratio, R, obtained from the decay curves is also shown.

Figure 4. The experimental excitation functions of the isomer ratio for the systems ^{128}Te + ^{12}C (open circles), ^{133}Cs + ^{7}Li (small stars), and ^{136}Ba + ^{3}He (open squares). The solid curves are the model predictions. The energy of the entrance channel is expressed in terms of the difference of the center-of-mass energy and the Coulomb barrier. Note that all three systems exhibit the saturation of R, albeit at different values of R. This difference in saturation value is explained in the text in terms of moments of inertia and entrance channel spins.

Figure 5. (a) The measured 3n fusion cross sections for the reaction $^{12}\mathrm{C} + {}^{128}\mathrm{Te} \rightarrow {}^{137}\mathrm{Ce} + 3\mathrm{n}$. The full curve is a calculation of the total fusion cross section as described in the text. The dashed curve shows the prediction for the 3n cross section, obtained with use of the predicted xn distributions. (b) The experimental isomer ratio. The full curve is a prediction based on the angular momentum distribution predicted by CCFUS and a statistical-decay calculation made with the code PACE. The predicted average angular momentum is indicated for selected bombarding

energies.

Figure 6. (a) The measured 2n fusion cross sections for the reaction ^{3}He + ^{136}Ba → ^{137}Ce + 2n. The full curve is a calculation of the total fusion cross section as described in the text. The dashed curve shows the prediction for the 2n cross section, obtained with use of the predicted xn distributions. (b) The experimental isomer ratio. The full curve is a prediction based on the angular momentum distribution predicted by CCFUS and a statistical-decay calculation made with the code PACE. The predicted average angular momentum is indicated for selected bombarding energies.

Figure 7. Theoretical predictions for the average angular momentum for fusion. The solid line is the prediction for a parabolic barrier and coupled channels (CCFUS). Using a parabolic barrier and no coupling in the entrance channel results in the dotted curve. The predictions for a nuclear-plus-Coulomb barrier and coupled channels are shown by the dashed curve [31]. Finally the results using a pure Coulomb barrier are shown by the dot-dashed curve.

Figure 8. Ratio of the d- and s-wave intensities (right ordinate) for the decay of $^{224\text{-}232}$Th [35]. The transition rates for the ground state decay, λ_0, are also shown (left ordinate) as a function of decay energy. The corresponding theoretical quantities, T_0 and $\frac{T_2}{T_0}$, calculated for a radius parameter $R_0 = 1.55$ fm [35] are also shown (dashed lines). The solid lines are to guide the eye.

Figure 9. The predicted angular momenta distributions for the fusion of ^{12}C + ^{128}Te obtained from the coupled channels model CCFUS. The center-of-mass

bombarding energy for each prediction is indicated on the figure. Notice that below the Coulomb barrier the shape of the σ_l distribution no longer changes and the mean value becomes a constant.

Figure 10. Several partial wave distributions used to investigate the sensitivity of the calculated isomer ratio to the shape of the angular momentum distribution. We investigated a delta function, a sharp-cutoff (Fermi) distribution, a rectangle, a Fermi function (dashed curve) and the CCFUS prediction. The resultant values of R are presented in Table VI.

Figure 11. Experimental (solid circles) and calculated isomer ratios (solid lines) for $^{12}C + ^{128}Te$ at $E_{c.m.} = 35$ and 40.5 MeV. This shows the dependence of the calculated value of R on the average angular momentum for a Fermi function with fixed Δl and variable l_0.

Figure 12. The observed isomer ratio (right ordinate) and the deduced $\bar{J}$ (left ordinate) for the system $^{12}C + ^{128}Te$.

Figure 13. The observed isomer ratio (right ordinate) and the deduced $\bar{J}$ (left ordinate) for the system $^{7}Li + ^{133}Cs$.

Figure 14. The observed isomer ratio (right ordinate) and the deduced $\bar{J}$ (left ordinate) for the system $^{3}He + ^{136}Ba$.

Figure 15. Experimental average angular momentum as a function of the excitation energy in the compound nucleus for all the systems studied in this work. Note the overlap of four different entrance channels in the region of excitation from 32 - 38

MeV.

Figure 16. The experimental isomer ratio for the system ^{12}C + ^{186}W as a function of the bombarding energy.

Figure 17. The sensitivity of the calculated isomer ratio to the angular momentum in the compound nucleus. The isomer ratio is calculated for a unique angular momentum (horizontal bar), a sharp-cutoff distribution as described in the text (dashed curve), and the same calculation shown in Fig. 5(b) (solid curve). The experimental values are indicated by the points with error bars.

Figure 18. The effects of spin-fractionation on the deduced $\overline{I}$. Three exit channels (2n, 3n, and 4n) are shown in (a) as a percentage of the total fusion cross section. The predicted $\overline{I}$ for the compound nucleus (solid line), 3n (dashed line), and pre-γ emission channels (dot-dashed line) are shown in (b).

Figure 19. Known low-spin levels (crosses), known high-spin levels (small stars) built on the isomer, and interpolated intermediate-spin levels (diamonds) in ^{137}Ce used in the statistical model calculations and discussed in text. The Yrast lines of Sierk (solid line) and of Gilbert-Cameron (dashed line) are also shown.

Figure 20. The effects of intermediate spin levels on the predicted isomer ratio. In (a) we show the three cases discussed in the text of adding six levels, using only the known levels, and using only the ground state and the isomer. In (b) we show the number and spin values of i) the known levels, ii) the six additional interpolated levels, and iii) a total of fourteen additional interpolated levels.

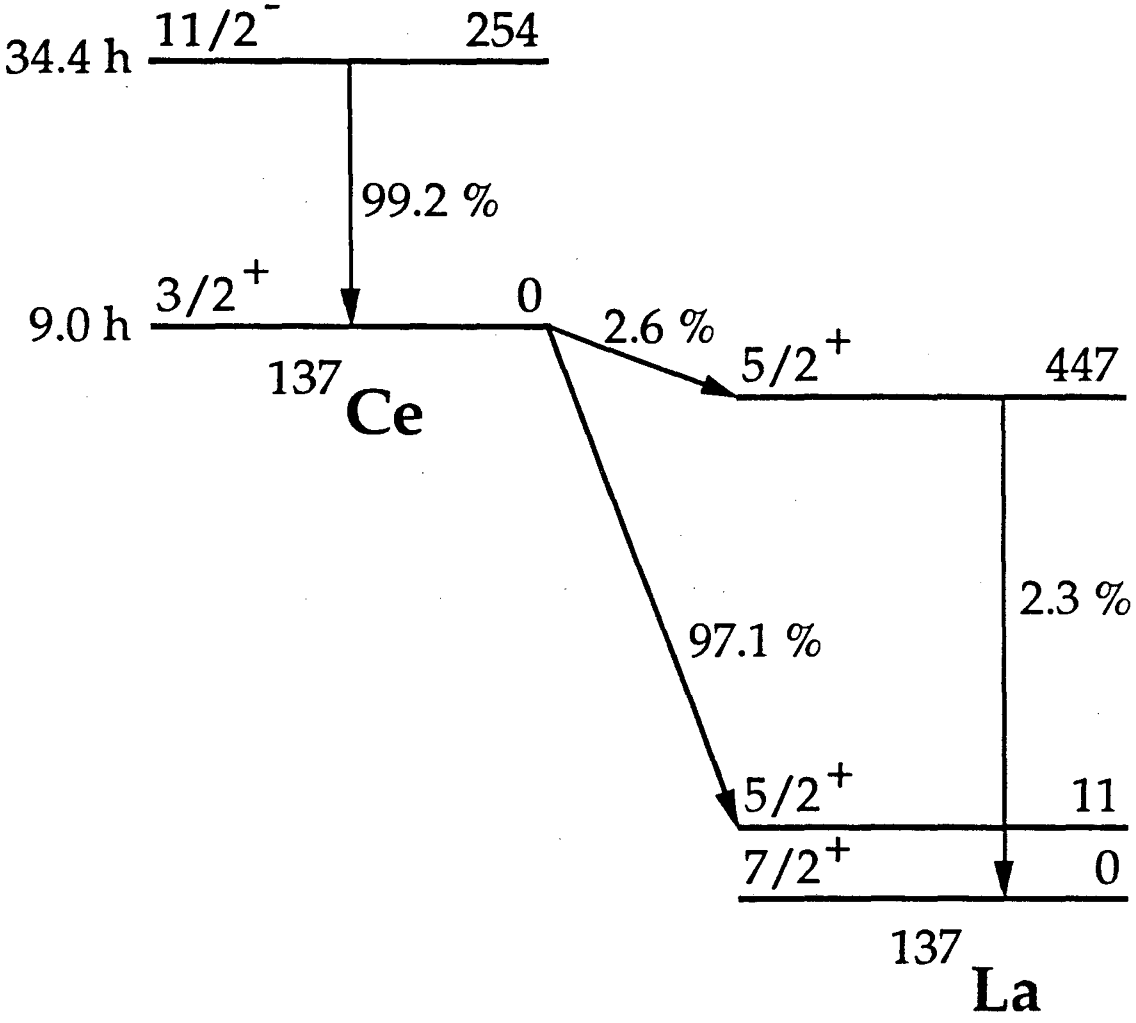

Figure 1

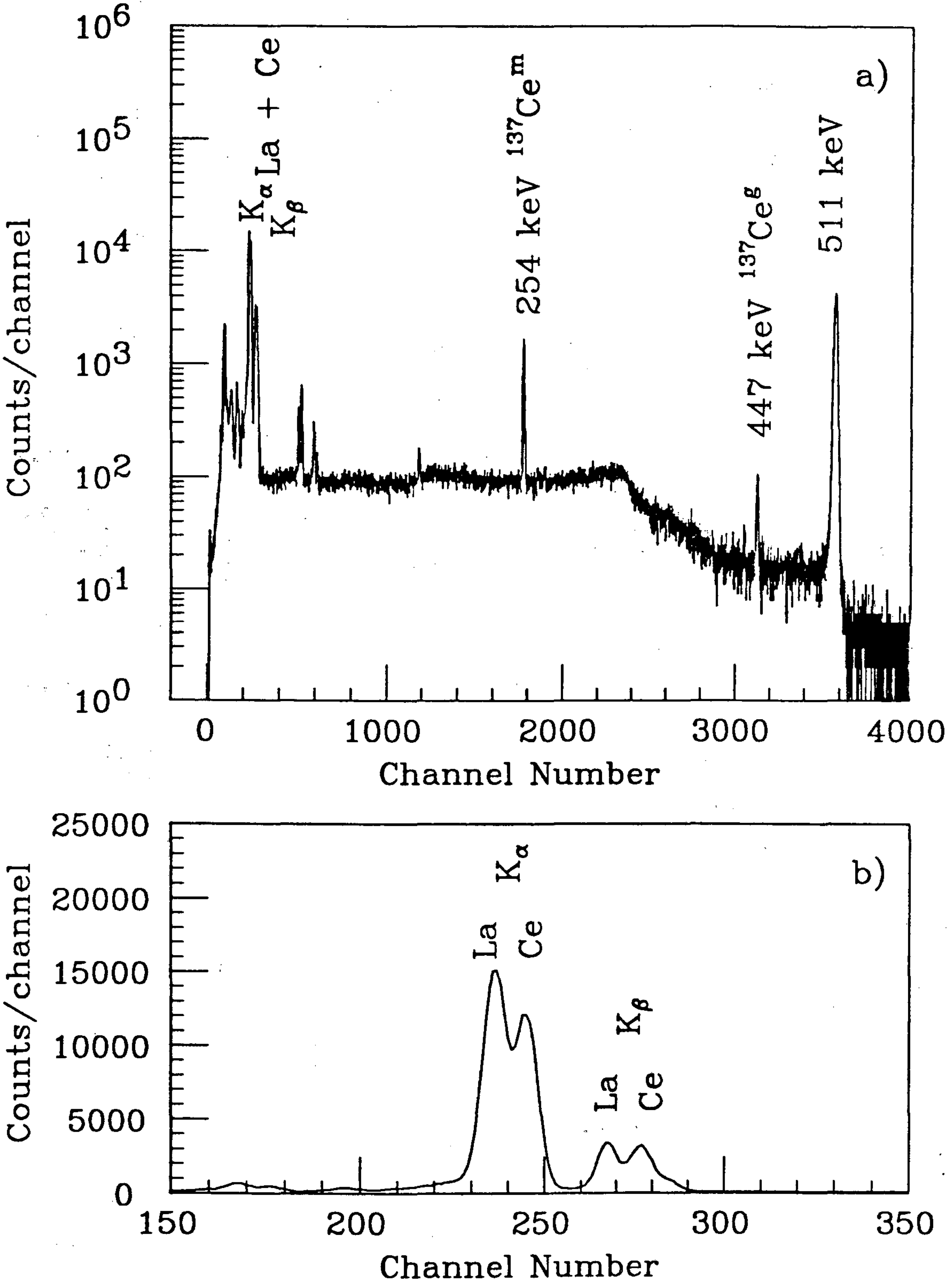
a)
Counts/channel
10^0
10^1
10^2
10^3
10^4
10^5
10^6
K_α La + Ce
K_β
254 keV ^{137}Ce^m
447 keV ^{137}Ce^g
511 keV
0
1000
2000
3000
4000
Channel Number
b)
Counts/channel
0
5000
10000
15000
20000
25000
K_α
La
Ce
K_β
La
Ce
150
200
250
300
350
Channel Number

Figure 2

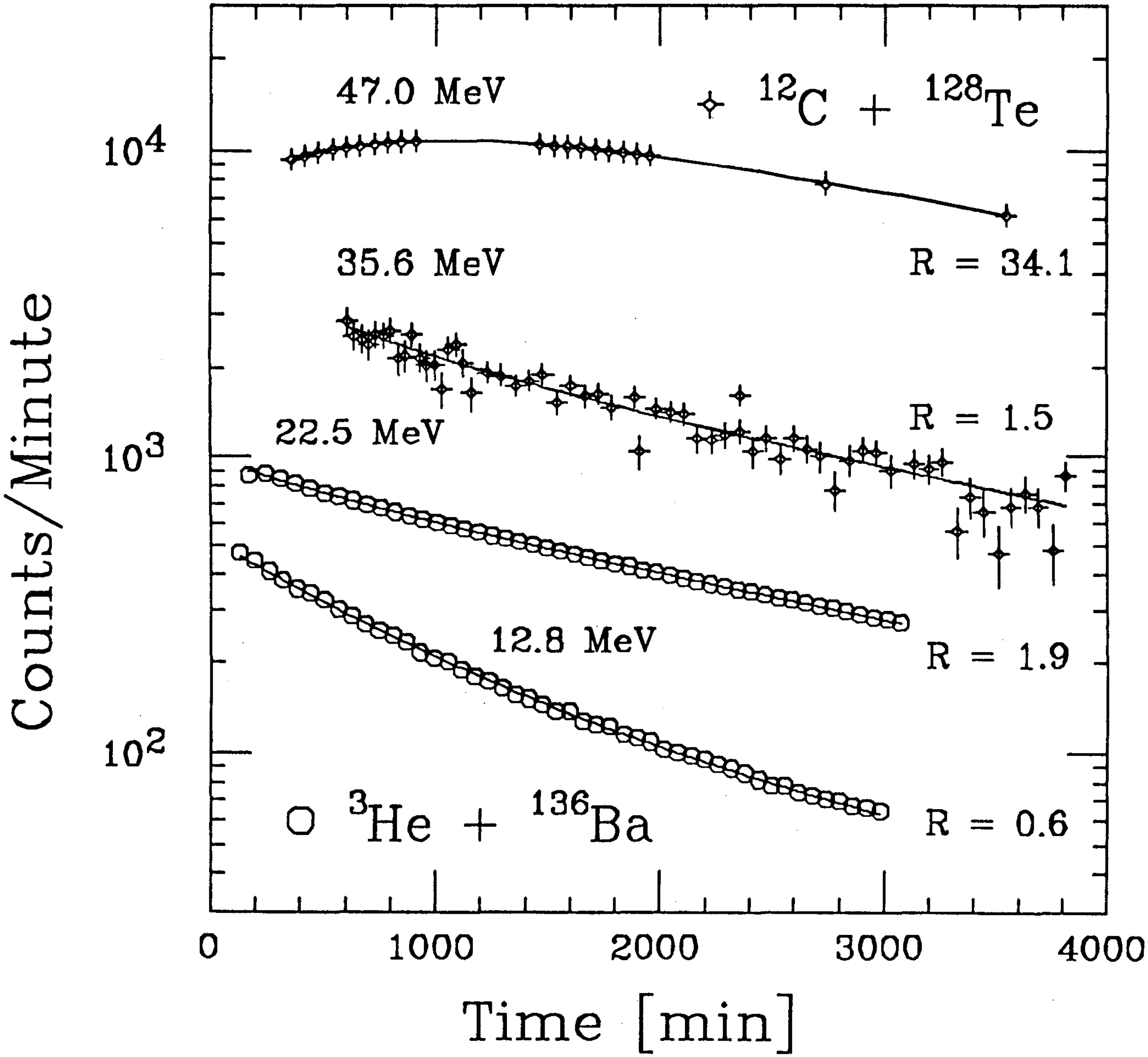
47.0 MeV
$^{12}C + ^{128}Te$
35.6 MeV
R = 34.1
R = 1.5
22.5 MeV
12.8 MeV
R = 1.9
R = 0.6
$^{3}He + ^{136}Ba$
10^4
10^3
10^2
Counts/Minute
0
1000
2000
3000
4000
Time [min]

Figure 3

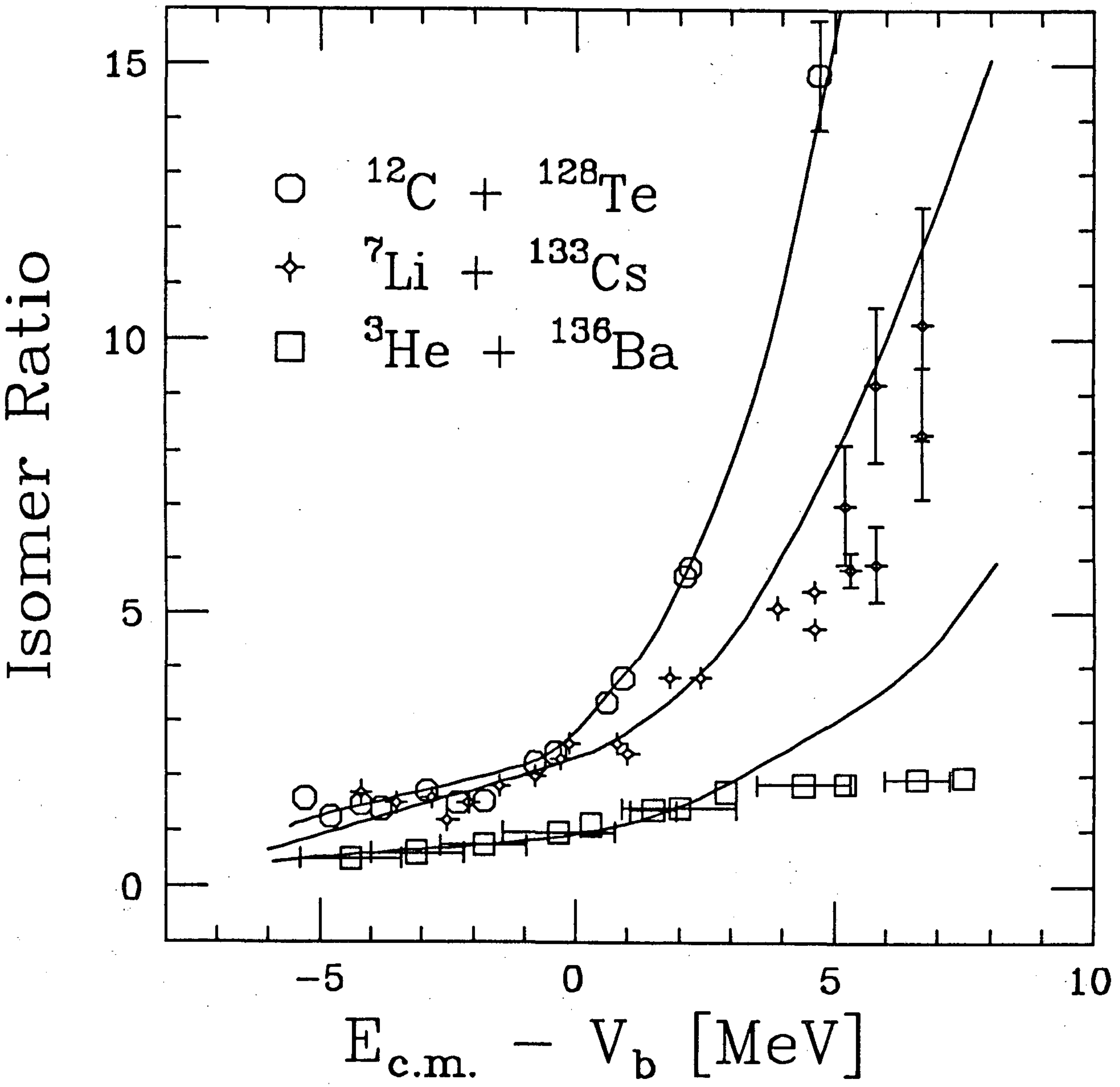
15
10
5
0
−5
0
5
10
Isomer Ratio
$E_{c.m.} - V_b$ [MeV]
$^{12}C + ^{128}Te$
$^{7}Li + ^{133}Cs$
$^{3}He + ^{136}Ba$

Figure 4

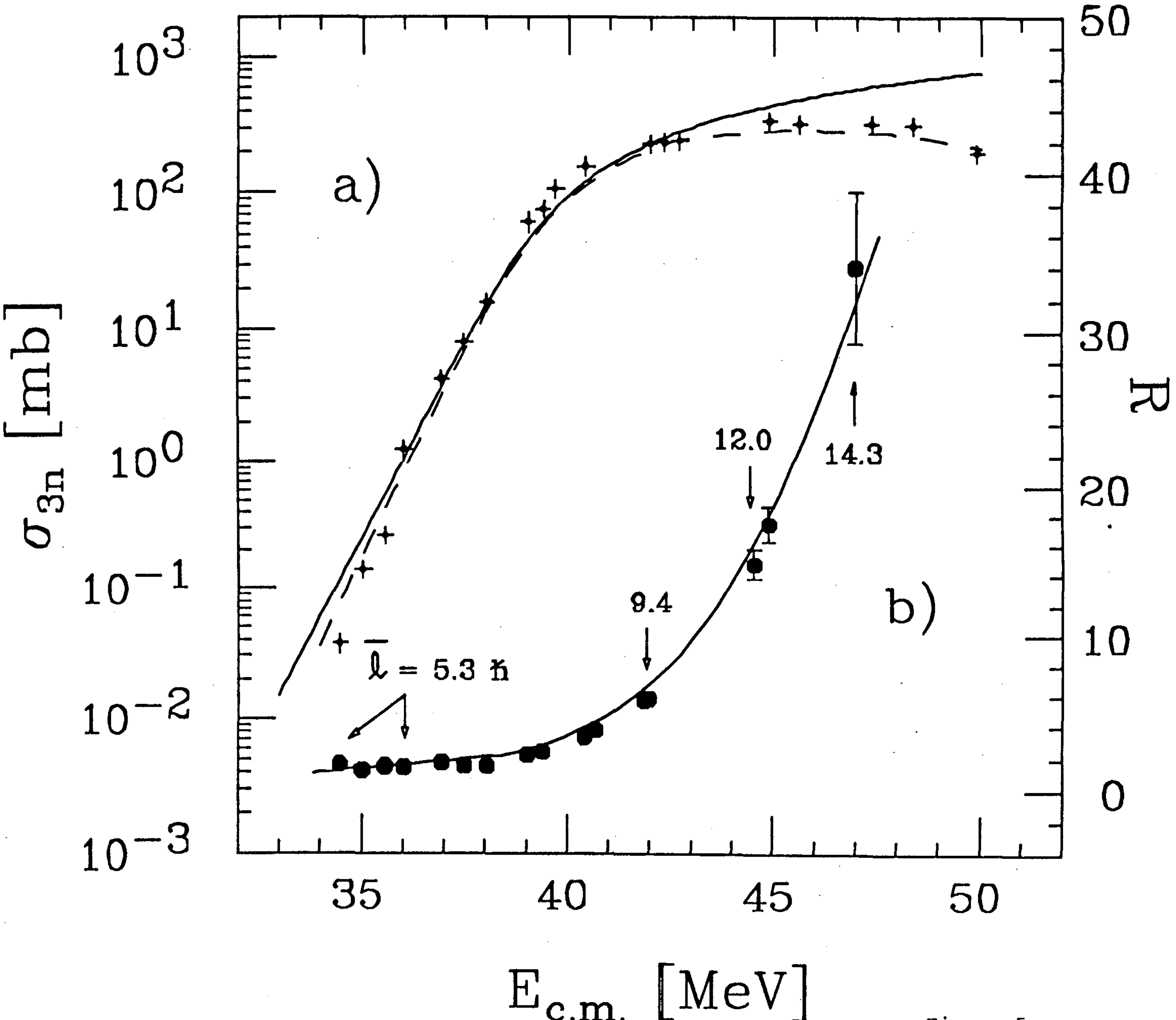
σ_{3n} [mb]
10^3
10^2
10^1
10^0
10^{-1}
10^{-2}
10^{-3}
a)
b)
$\bar{\ell}$ = 5.3 ħ
9.4
12.0
14.3
R
50
40
30
20
10
0
35
40
45
50
$E_{c.m.}$ [MeV]

Figure 5

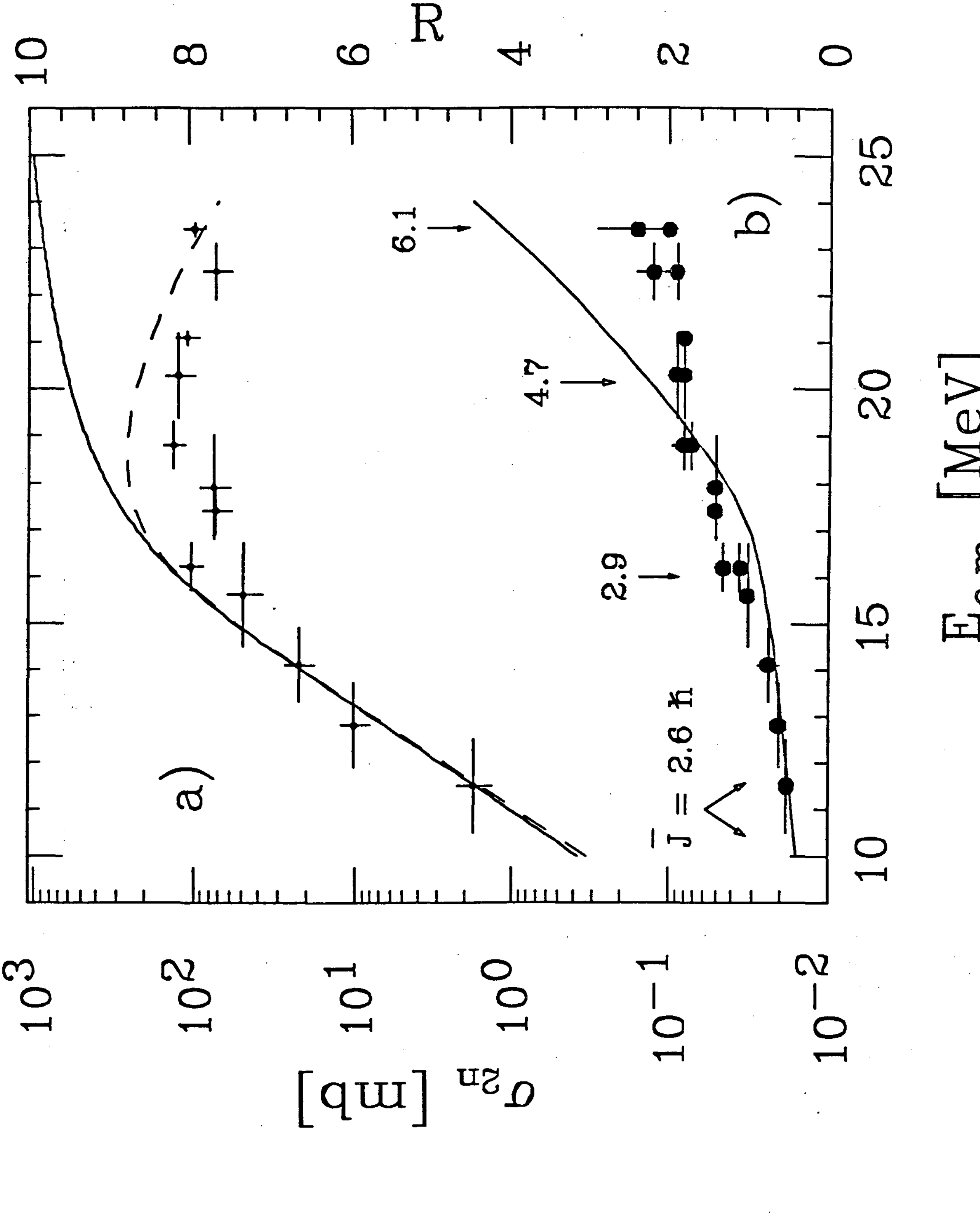

σ_{2n} [mb]
10^3
10^2
10^1
10^0
10^{-1}
10^{-2}
R
10
8
6
4
2
0
a)
b)
$\bar{J} = 2.6\ \hbar$
2.9
4.7
6.1
10
15
20
25
$E_{c.m.}$ [MeV]

Figure 6

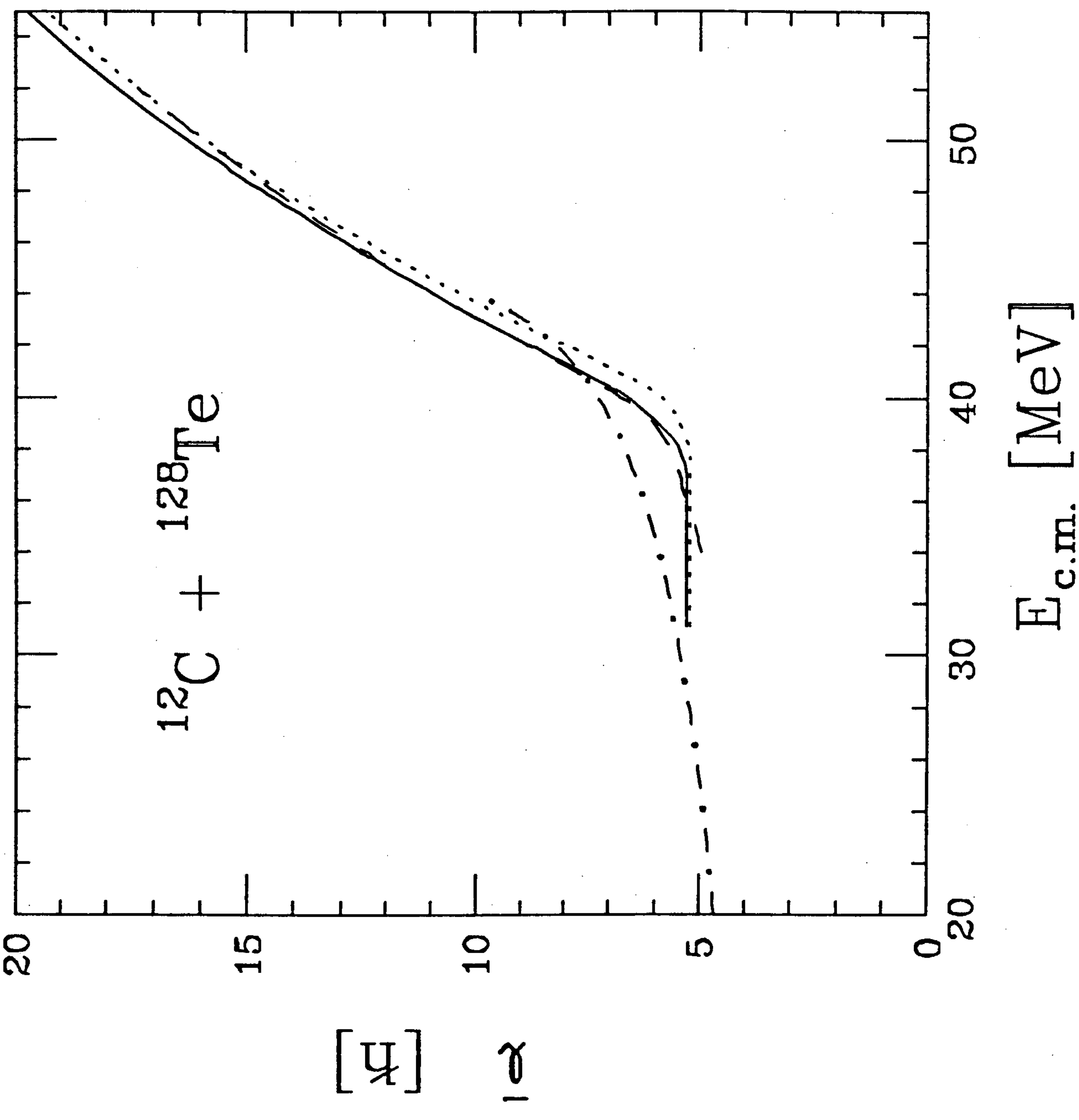

Figure 7

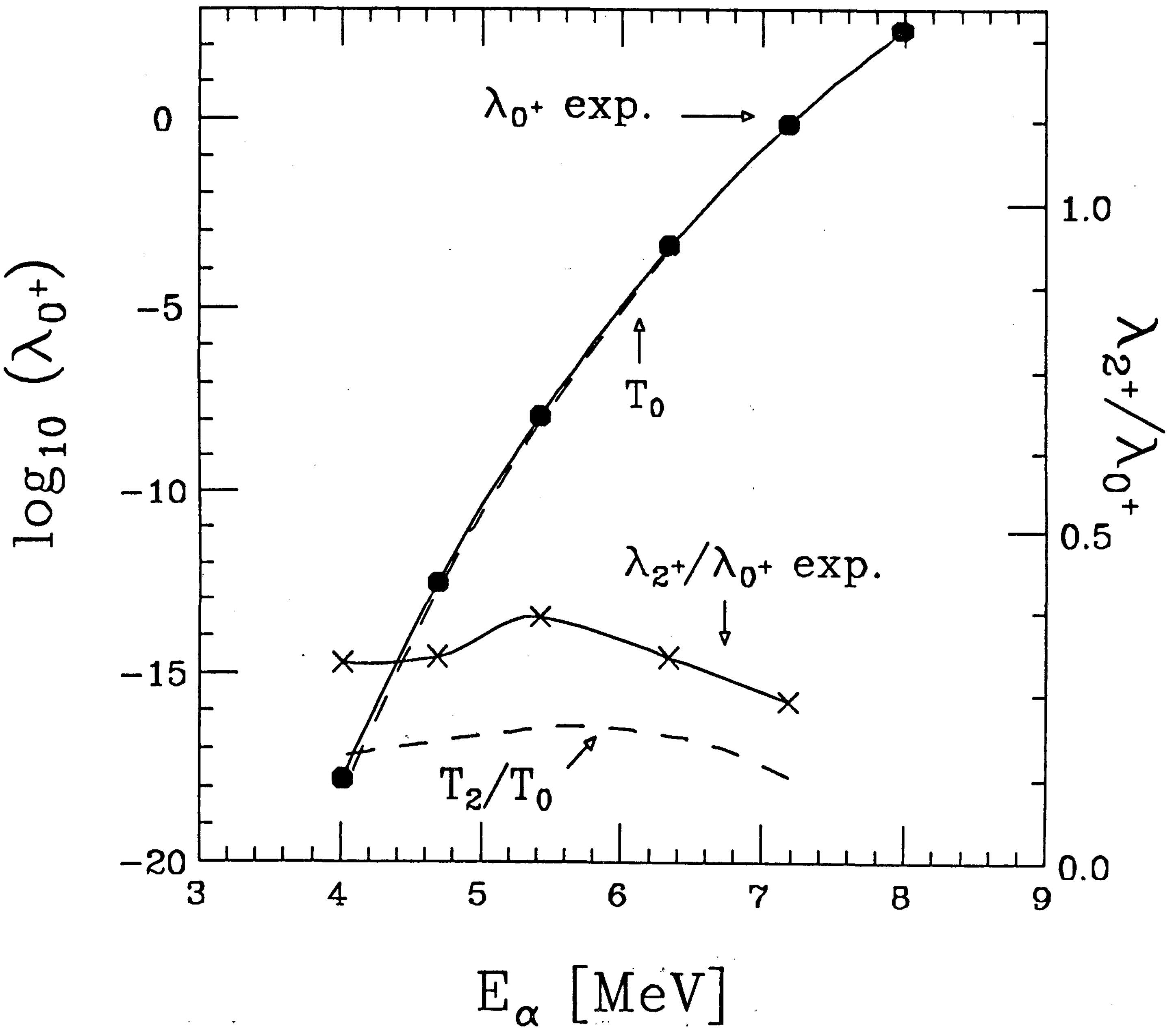$\log_{10}(\lambda_{0^+})$
0
-5
-10
-15
-20
3
4
5
6
7
8
9
E_α [MeV]
$\lambda_{2^+}/\lambda_{0^+}$
1.0
0.5
0.0
λ_{0^+} exp.
T_0
$\lambda_{2^+}/\lambda_{0^+}$ exp.
T_2/T_0

Figure 8

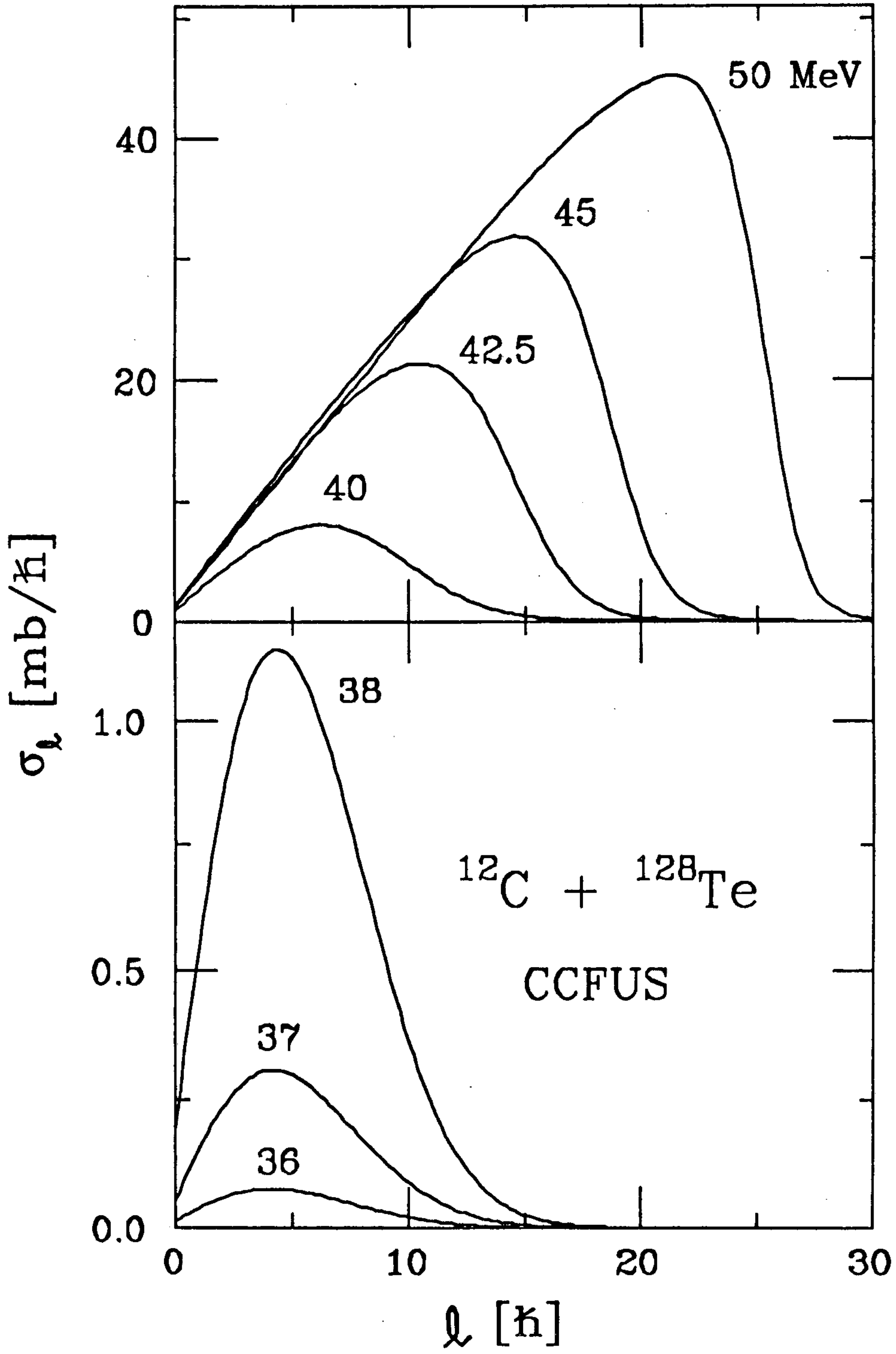
50 MeV
45
42.5
40
38
37
36
40
20
0
1.0
0.5
0.0
0
10
20
30
σ_ℓ [mb/ħ]
ℓ [ħ]
¹²C + ¹²⁸Te
CCFUS

Figure 9

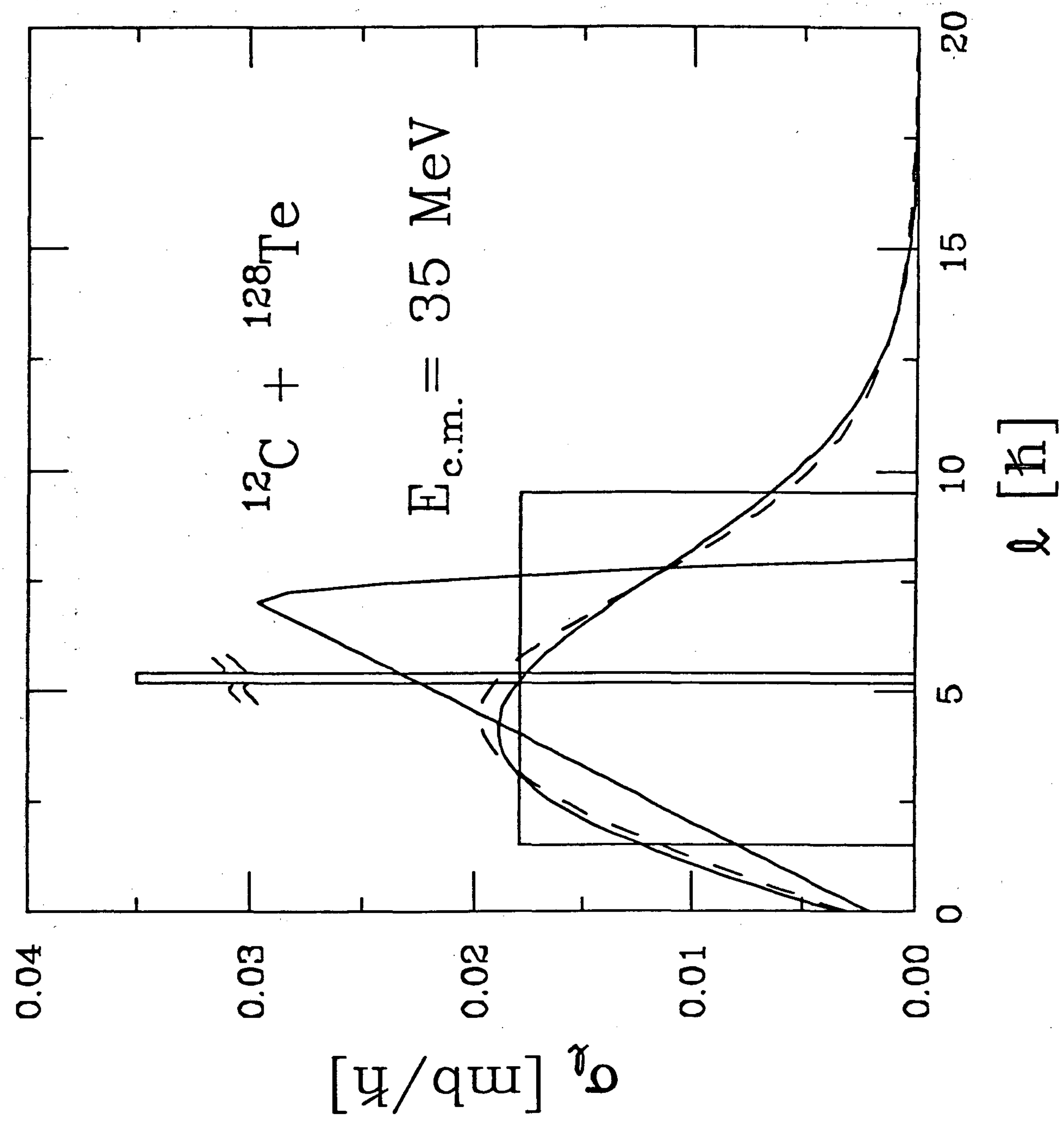

$^{12}C + ^{128}Te$
$E_{c.m.} = 35$ MeV
σ_ℓ [mb/ħ]
0.04
0.03
0.02
0.01
0.00
0
5
10
15
20
ℓ [ħ]

Figure 10

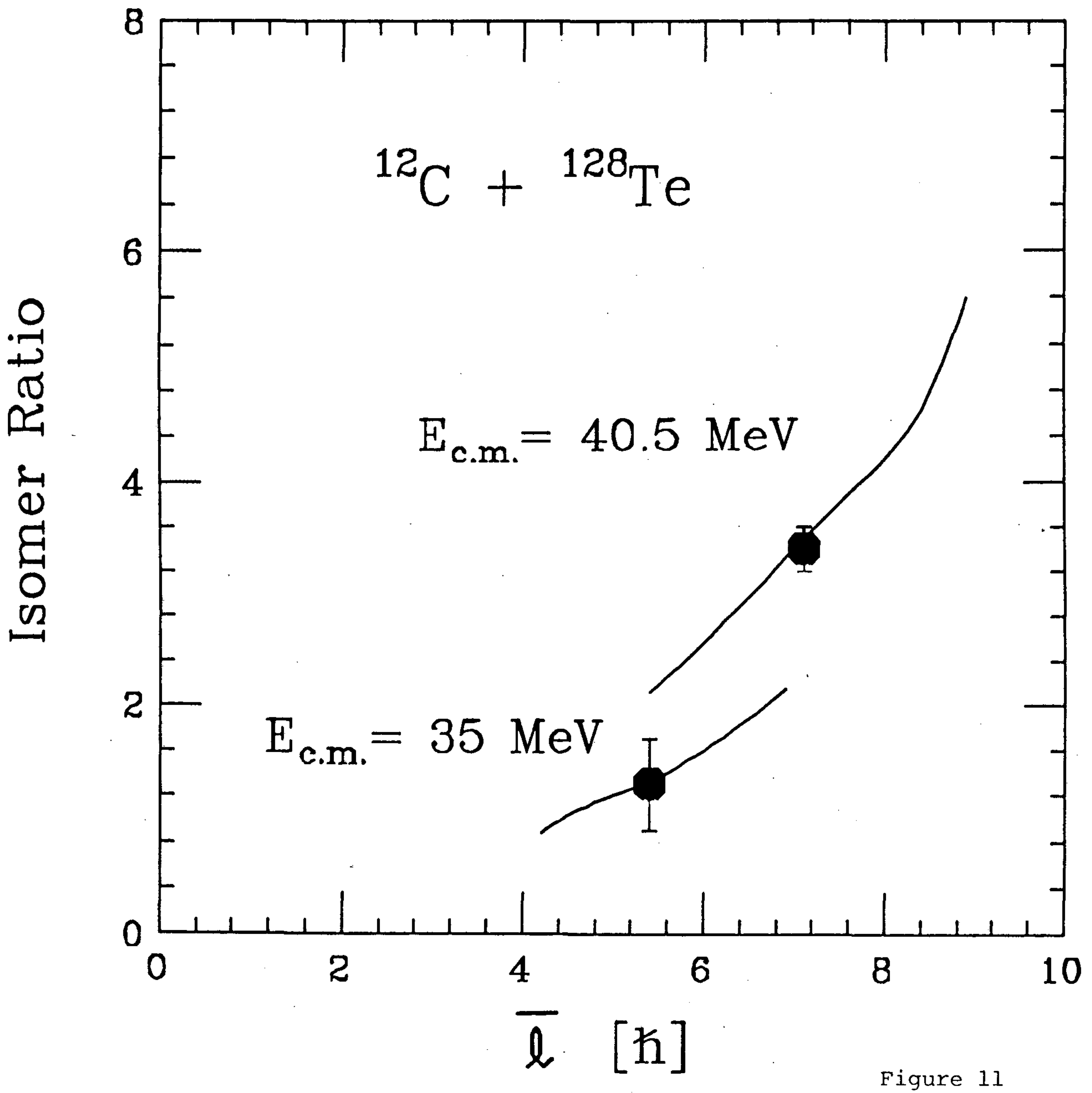
Isomer Ratio
0
2
4
6
8
0
2
4
6
8
10
$\overline{\ell}$ [ℏ]
^{12}C + ^{128}Te
$E_{c.m.}$= 40.5 MeV
$E_{c.m.}$= 35 MeV

Figure 11

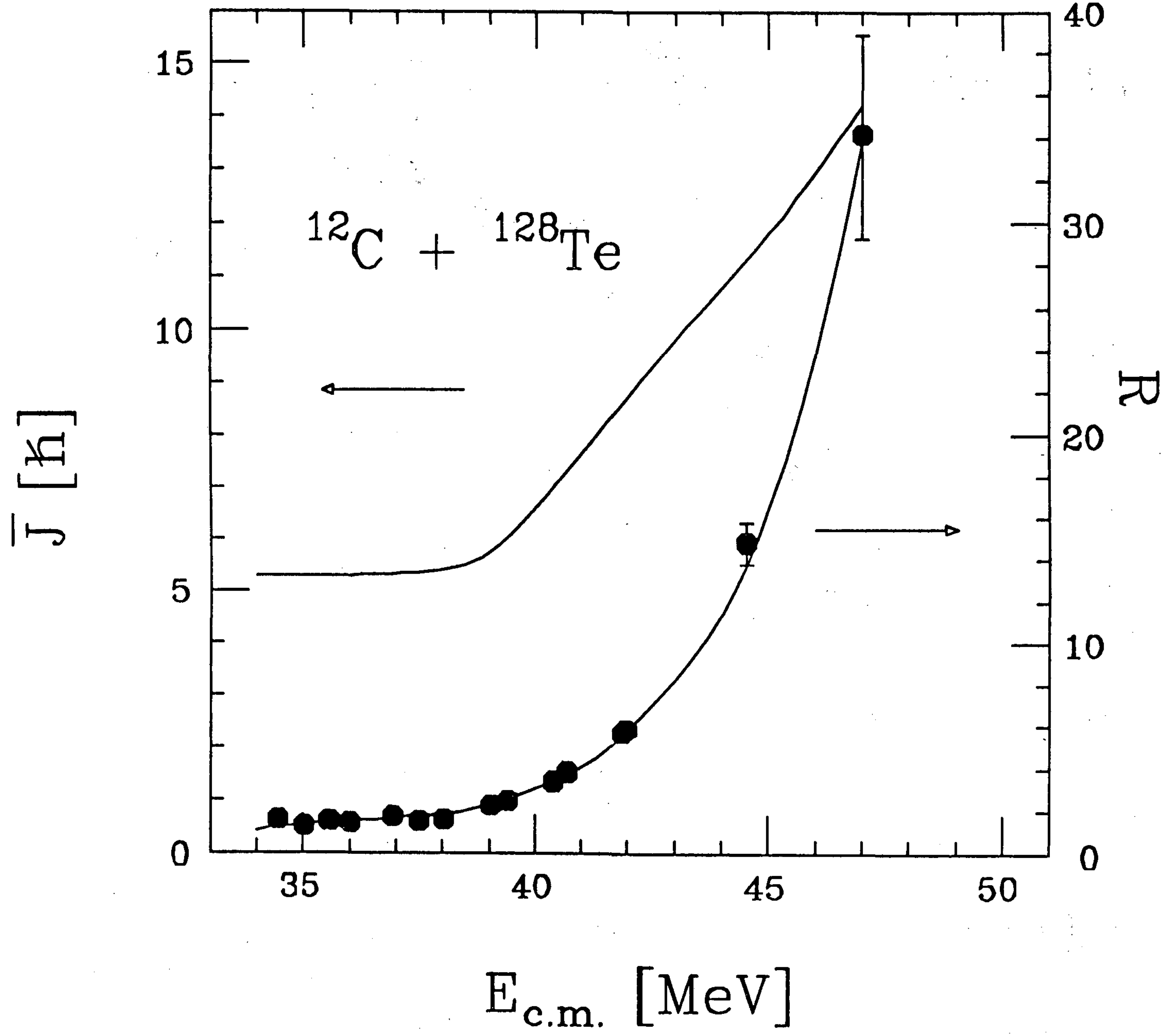

Figure 12

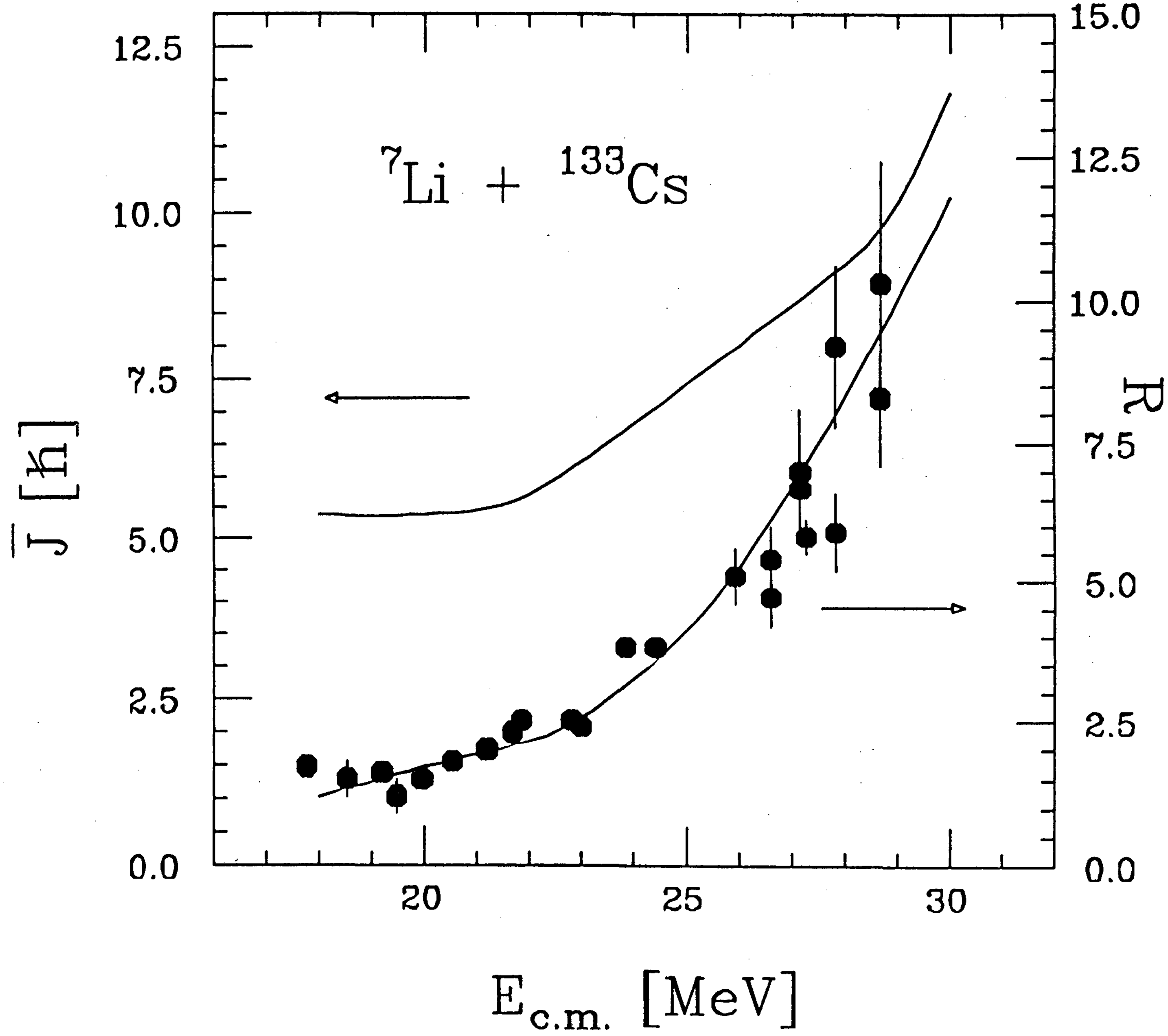

Figure 13

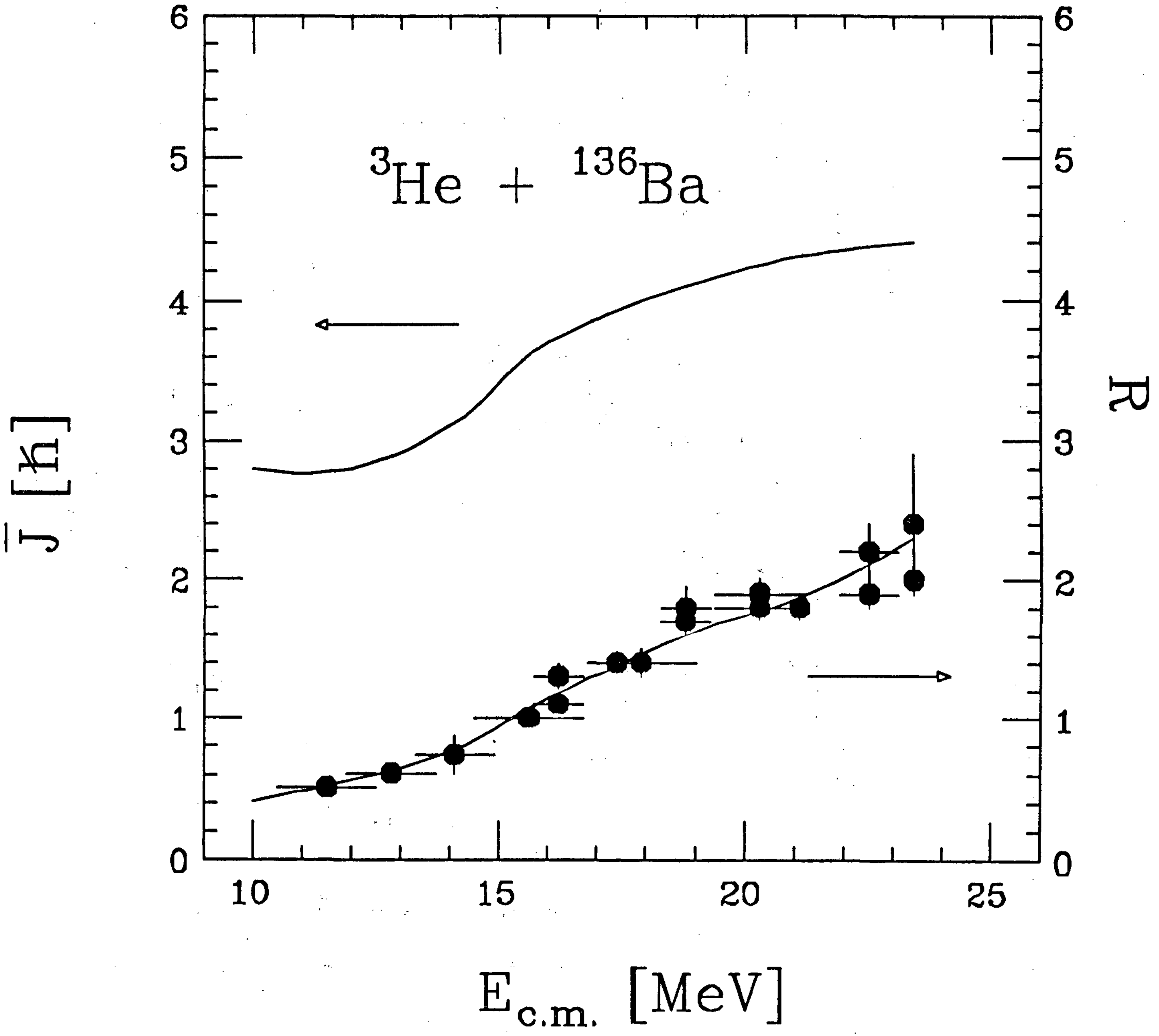

Figure 14

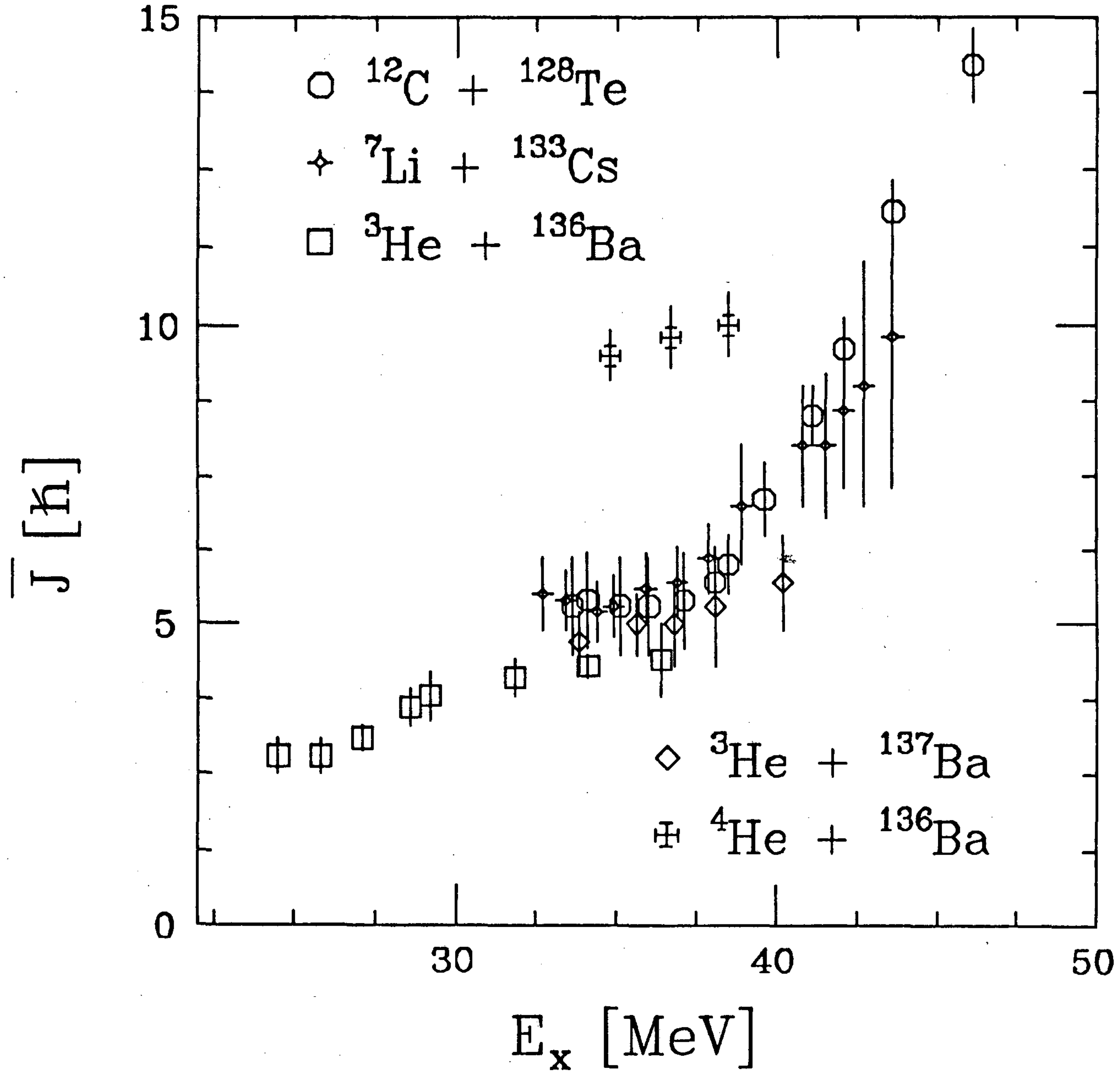
15
10
5
0
30
40
50
$\overline{J}$ [ħ]
E_x [MeV]
$^{12}C + ^{128}Te$
$^{7}Li + ^{133}Cs$
$^{3}He + ^{136}Ba$
$^{3}He + ^{137}Ba$
$^{4}He + ^{136}Ba$

Figure 15

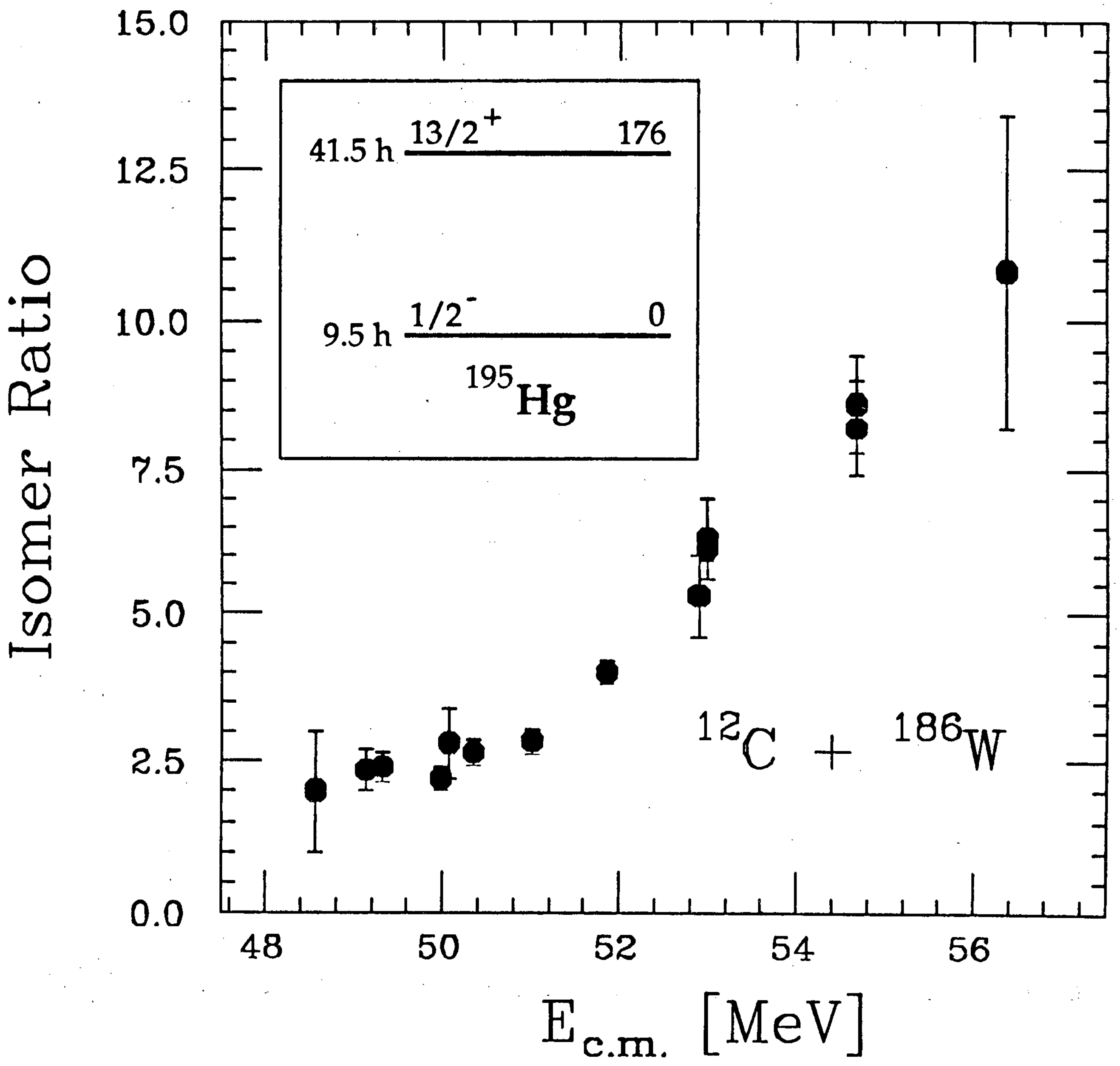
Isomer Ratio
15.0
12.5
10.0
7.5
5.0
2.5
0.0
48
50
52
54
56
E c.m. [MeV]
41.5 h
13/2+
176
9.5 h
1/2-
0
195Hg
12C + 186W

Figure 16

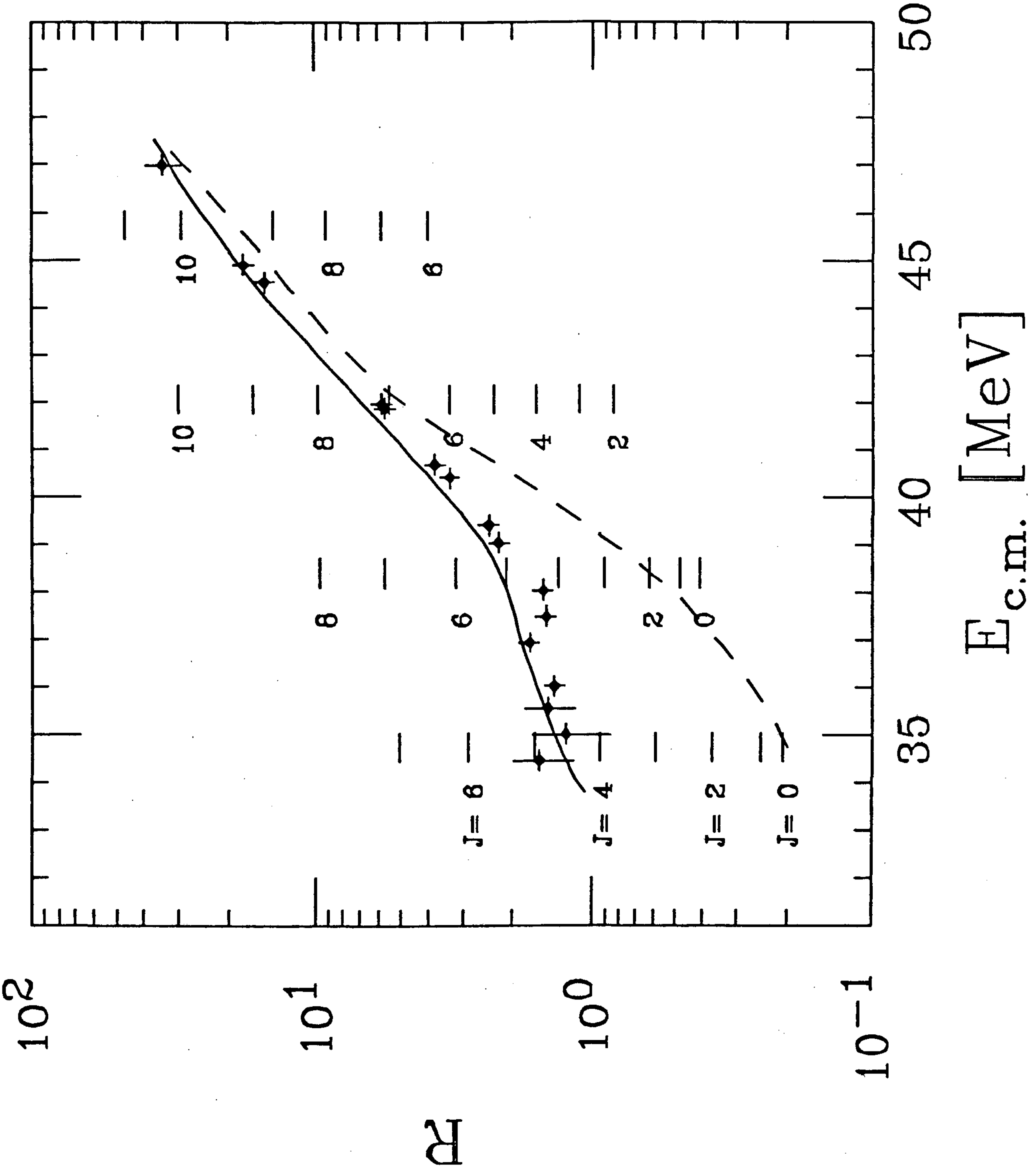

Figure 17

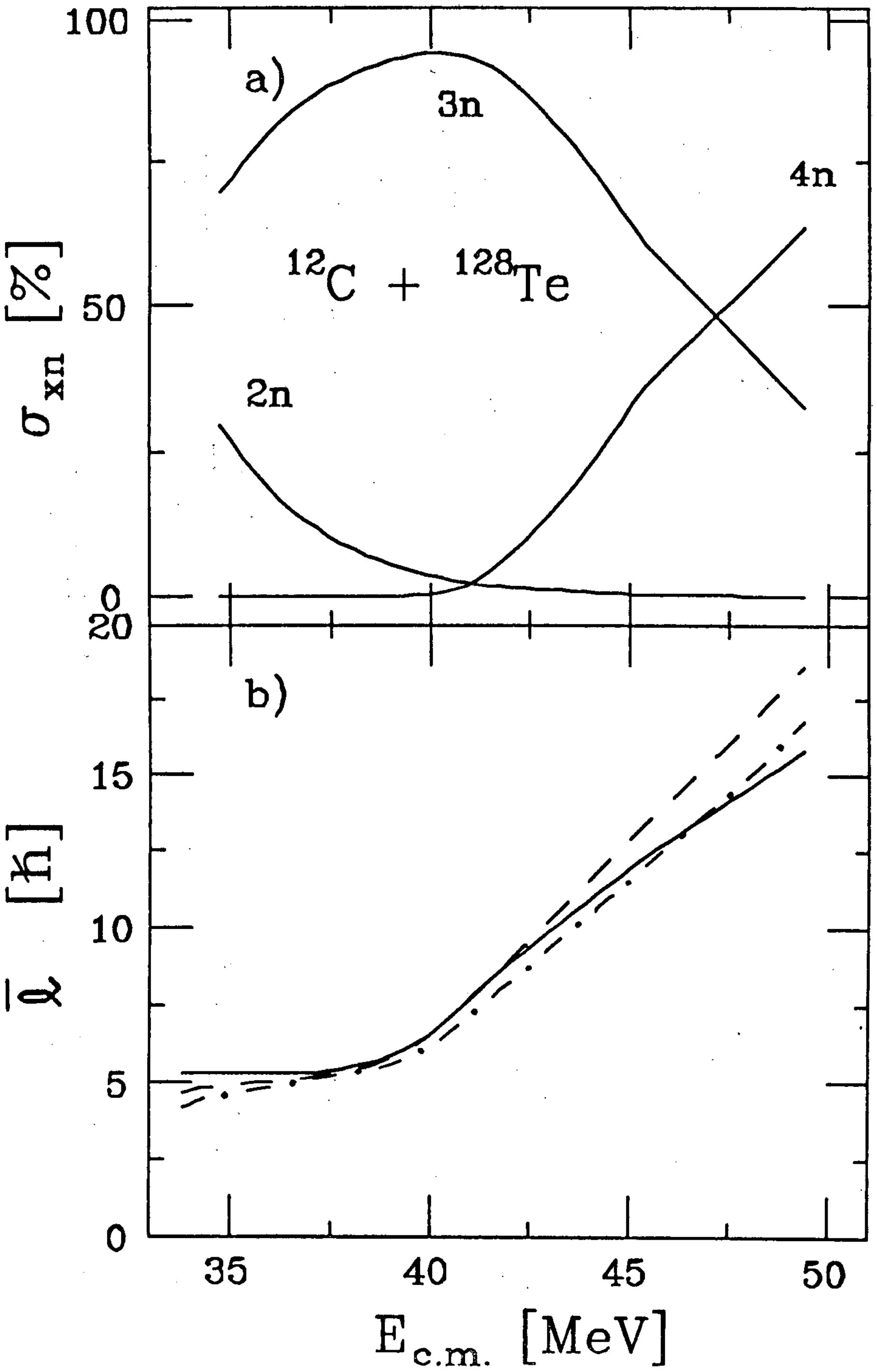
a)
3n
4n
2n
$^{12}C + ^{128}Te$
σ_{xn} [%]
100
50
0
20
b)
15
10
5
0
$\bar{\ell}$ [ħ]
35
40
45
50
$E_{c.m.}$ [MeV]

Figure 18

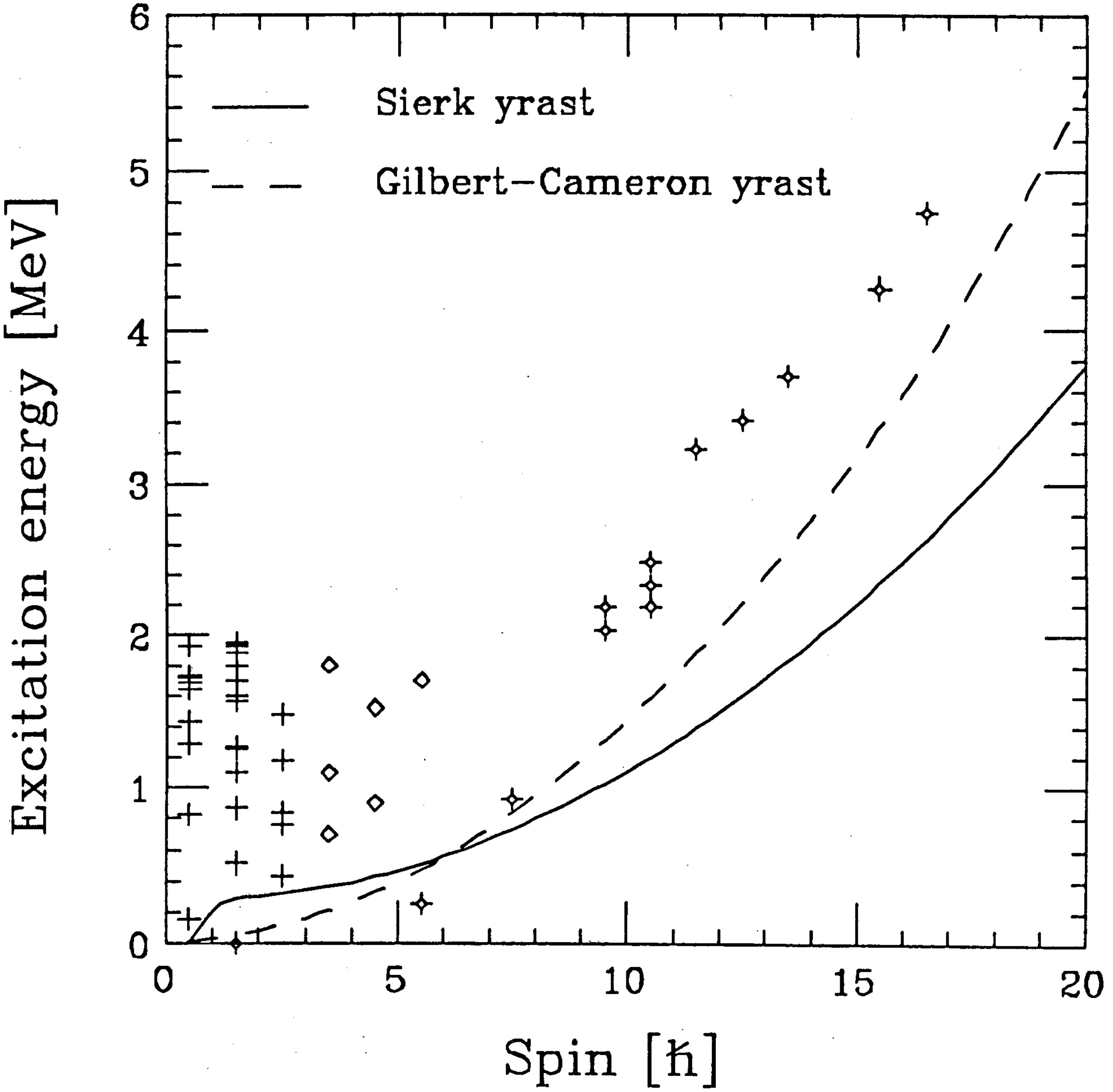
Sierk yrast
Gilbert–Cameron yrast
Excitation energy [MeV]
Spin [ħ]
0
1
2
3
4
5
6
0
5
10
15
20

Figure 19

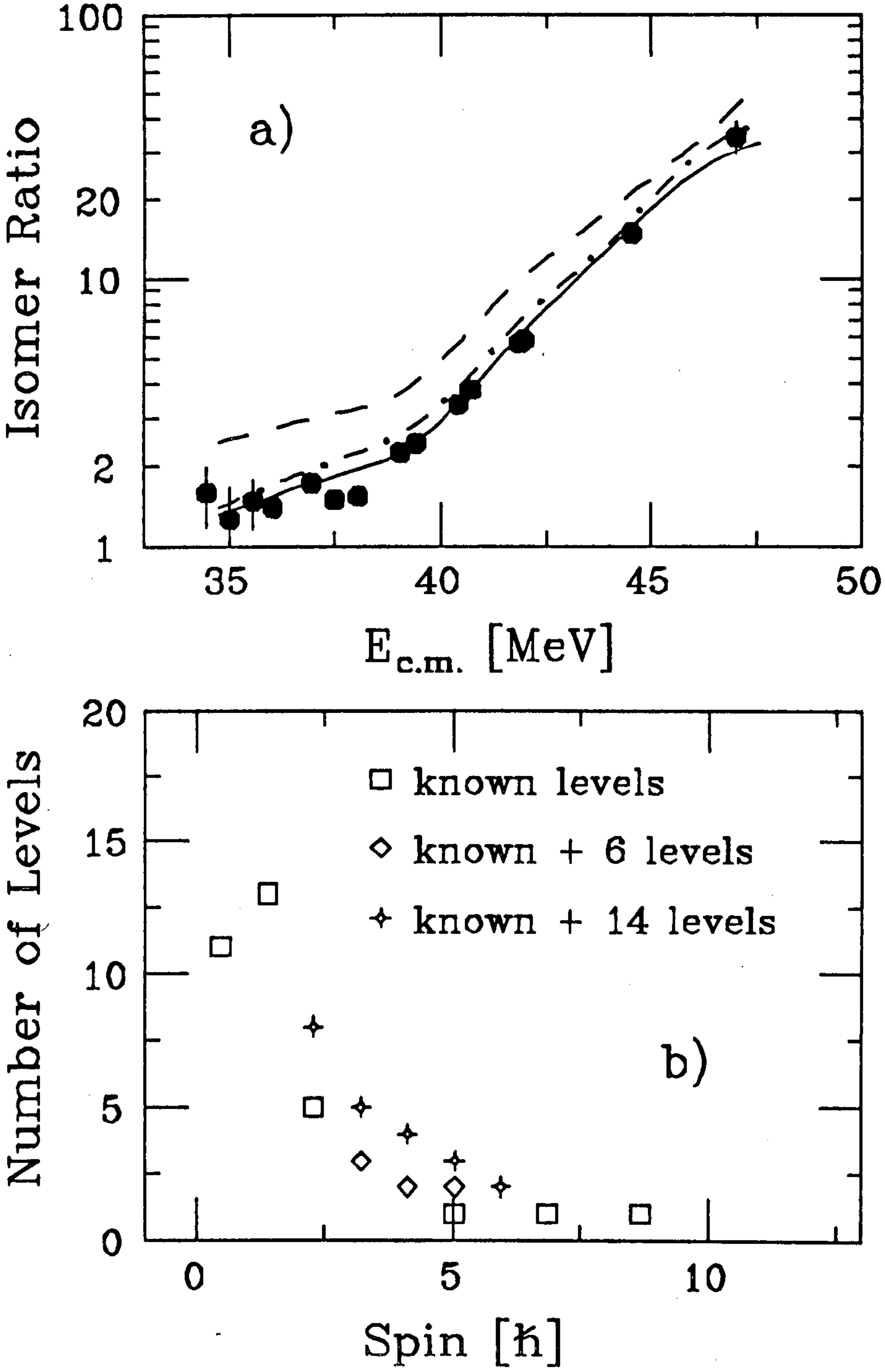
a)
Isomer Ratio
100
20
10
2
1
35
40
45
50
$E_{c.m.}$ [MeV]
b)
Number of Levels
20
15
10
5
0
0
5
10
Spin [ħ]
□ known levels
◇ known + 6 levels
✦ known + 14 levels

Figure 20

LAWRENCE BERKELEY LABORATORY
UNIVERSITY OF CALIFORNIA
INFORMATION RESOURCES DEPARTMENT
BERKELEY, CALIFORNIA 94720